THESIS

RADIATION CHARACTERIZATION AT LASER WAKEFIELD ACCELERATORS

Submitted by

Soren Baines Clawson

Department of Environmental and Radiological Health Sciences

In partial fulfillment of the requirements

For the Degree of Master of Science

Colorado State University

Fort Collins, Colorado

Summer 2025

Master's Committee:

Advisor: Alexander Brandl

Thomas Johnson
Michael Mooney
Jenelle Mann

ABSTRACT

RADIATION CHARACTERIZATION AT LASER WAKEFIELD ACCELERATORS

Laser wakefield acceleration (LWFA) is a rapidly evolving technology that enables the compact acceleration of electrons to relativistic velocities using intense, high repetition laser pulses in plasma. These high-energy electrons interact with surrounding materials to produce complex, pulsed radiation fields composed of bremsstrahlung photons, neutrons, and in some cases, exotic mesons and leptons. Accurately characterizing these radiation environments is essential for radiation protection and facility safety planning in LWFA environments. This thesis presents a computational framework for estimating the spectral distributions of secondary radiation generated by monoenergetic electron beams. The geometric basis of the simulations presented is of the Advanced Beam Laboratory, room 103, at Colorado State University. Using the Monte Carlo N-Particle (MCNP) transport code, a two-stage simulation approach was developed to mitigate inefficiencies in electron transport. In the first stage, electron interactions in a tungsten target were used to construct angle- and energy-resolved photon spectra, as photons are the primary generator of mesons, leptons, and neutrons. These photon distributions were then used as sources in secondary simulations to estimate effective dose from photons and neutrons throughout the laboratory environment. Near the main laboratory entrance, for a 10 pC bundle of accelerated electrons accelerated between 100 MeV and 10 GeV, combined photon and neutron effective doses are found to range between 2.69 pSv and 506 pSv. This method accounts for directional asymmetries in emission, uncertainty propagation, and applies fluence-to-dose conversion factors for photon and neutron fluences at point detectors. Results include dose estimates per incident electron as a function of beam energy. This study supports the development of predictive dose models and provides data-driven tools for the for the design of radiological controls in future high-energy LWFA experiments.

ACKNOWLEDGEMENTS

First and foremost, I would like to thank my wonderful fiancée, Meghan Roelse. Whose continued support and encouragement through my graduate studies provided the drive and confidence to complete this program. I could not have done it without you. Second, I would like to acknowledge my parents, Susan and Stephen Clawson, for pushing me to strive for the most, despite the associated tribulations. It was nine short years ago that we doubted if I had it in me to even graduate high school. Your unconditional love and guidance drove me to the position I am in today. Next, my great friend and colleague, Noah Blair, who encouraged me to pursue graduate studies in health physics, taught me how to be a successful graduate student, and of course, provided the MCNP parsing code that carried me through my research. Finaly, I would like to acknowledge my advisor, Alex Brandl, the Brandl research group, and the rest of the students and faculty in the health physics program, for aiding me through this program and offering support where my abilities fell short, or so I thought.

DEDICATION

To my grandfather, Alden Ernest Clawson.

Thank you for catalyzing my interest in scientific discovery and encouraging my continued interest in physics and mathematics. I miss you dearly every day.

TABLE OF CONTENTS

ABSTRACT ii
ACKNOWLEDGEMENTS iii
DEDICATION iv
LIST OF TABLES vii
LIST OF FIGURES viii

Chapter 1 Introduction 1
1.1 Project Overview 1
1.1.1 Historical Overview 2
1.1.2 Laser Wakefield Acceleration 2
1.1.3 Applications at Colorado State University 3
1.2 Radiation and Particle Interactions 4
1.2.1 Electron Interactions 5
1.2.2 Photon and Neutron Interactions 7
1.3 Dose and Radiation Protection Considerations 11
1.3.1 Definition of Radiation Dose 11
1.3.2 Dosimetric Considerations for LWFA Facilities 13
1.3.3 Calibration and Instrumentation Challenges 14
1.3.4 Photon vs. Neutron Dosimetry 14
1.4 Monte Carlo N-Particle Transport Code 15
1.4.1 Overview and Capabilities 16
1.4.2 Electron Transport in MCNP 17
1.5 Project Goals 18

Chapter 2 Methodology 19
2.1 Methodology Overview 19
2.2 MCNP Simulation Setup 20
2.2.1 MCNP Geometry and Materials 20
2.2.2 Interaction Data 22
2.2.3 Physics Models 22
2.2.4 F2 Tallies and Bins 23
2.2.5 F5 Tallies, and Dose 24
2.3 Source Specifications 24
2.3.1 The Piece Wise Approach 24
2.3.2 Primary Electron Source 26
2.3.3 Secondary Photon Source 28
2.4 Data Analysis 30
2.4.1 Use of Iterated MCNP Runs 30
2.4.2 Uncertainty Propagation 30
2.4.3 Fluence Combination for Multiple Runs 32
2.4.4 Obtaining Distributions of Photons Generated 33

2.4.5 Obtaining Angular Photon Distributions . . . 33
2.4.6 Angular and Energetic Probability Distributions . . . 37
2.5 Input Generation and Output Processing . . . 38

Chapter 3 Results . . . 39
3.1 Checks for Lateral Photon Emission Homogeneity . . . 39
3.2 Photon Probability Distributions . . . 40
3.2.1 Energy Distributions . . . 40
3.2.2 Angular Distributions . . . 42
3.3 Particle Production . . . 43
3.4 Ambient Dose Calculations . . . 44

Chapter 4 Discussion . . . 45
4.1 Azimuthal Symmetry in Lateral Photon Emission . . . 45
4.2 Probability Density Functions . . . 45
4.2.1 Energy Distributions . . . 45
4.2.2 Angular Distributions . . . 46
4.3 Particle Generation . . . 48
4.4 Dosimetry and Neutron Activation Concerns . . . 49

Chapter 5 Conclusion . . . 52

Appendix A Data . . . 59

LIST OF TABLES

1.1 Decay characteristics of select mesons and leptons. 10
1.2 Standard tallies available in MCNP 16

2.1 MCNP-assigned surface numbers, associated normal vectors, and classifications as lateral or incident. 34
2.2 Angular transformations applied to tally data. Lateral angles are shifted relative to the surface normal to align with the beamline direction. No transformation is needed for forward-going incident fluence. 35

4.1 Number of photons and neutrons generated per source electron. 48
4.2 Estimated total effective dose (pSv) per 10 pC monoenergetic electron bundle, by detector position and source energy. Note that the beam is directed 60° north of east. Energies are given in MeV. 50

A.1 Isotopic composition of materials used in MCNP by nuclide and atom fraction. 59
A.2 Photonuclear cross-section library information for materials. 61
A.3 Nuclear cross-section library information for materials. 63
A.4 Effective dose per fluence for mono-energetic photons incident on anteroposterior geometry. 65
A.5 Effective dose per fluence for mono-energetic neutrons incident on anteroposterior geometry. 67

LIST OF FIGURES

1.1 Diagram illustrating the process of bremsstrahlung emission by an electron interacting with an atomic nucleus. . . . 6
1.2 Plot of neutron radiation weighting factors vs. energy. . . . 12

2.1 MCNP geometry as seen from two perspectives, colored by material type. (a) Top-down full view (xy-plane). (b) Side full view (yz-plane). (c) Zoomed top-down view. (d) Zoomed side view. (e) Material color legend. . . . 21
2.2 Plot of fluence-to-dose conversion data from ICRP 116 for monoenergetic neutrons incident on AP geometry. . . . 25
2.3 Plot of fluence-to-dose conversion data from ICRP 116 for monoenergetic photons incident on AP geometry. . . . 25
2.4 Plot of fluence-to-dose conversion data from ICRP 116 for monoenergetic electrons incident on AP geometry. . . . 26
2.5 Simplified electron source geometry. Electrons are emitted from the center toward the tungsten target, colored magenta. . . . 28
2.6 Image of the xz-plane, showcasing the full geometry of the photon simulations, including the external tally sphere. . . . 29
2.7 Illustration of a photon exiting surface 100.1 of the tungsten block, where the surface normal is $\hat{n}(100.1) = +\hat{x}$. The photon is recorded as contributing to the bin defined by polar angle α_2, but its azimuthal angle remains unspecified. . . . 35
2.8 Illustration of angular rearrangement procedure. (a) Angle transformation for lateral fluences attributed to the forward direction. (b) Angle transformation for lateral fluences attributed to the backward direction. (c) Angle transformation for incident fluences through the $-\hat{y}$ surface. . . . 36

3.1 Kernel density estimate plot of t-distributions by electron source energy for $\pm x$ surfaces. 39
3.2 Kernel density estimate plot of t-distributions by electron source energy for $\pm z$ surfaces. 40
3.3 Normalized photon energy spectra, shown as probability density functions per MeV for each electron source energy. . . . 41
3.4 Normalized angular spectra of emitted photons, with polar emission angle ranging from 0 radians (forward, aligned with beamline) to π radians (backward, antiparallel). . 42
3.5 Number of secondary particles (photons and neutrons) produced per source electron entering the tungsten target. . . . 43
3.6 Total effective dose (pSv) per 10 pC electron bundle at 100 MeV and 1 GeV source energies. Top: full detector regions. Bottom: zoomed-in regions near the beamline. . . 44

4.1 Smoothed angular spectra of emitted photons using local regression; normalized probability density per radian. . . . 47

Chapter 1

Introduction

1.1 Project Overview

Modern particle accelerators represent a convergence of advanced engineering and applied physics, enabling frontier research in high-energy physics, materials science, and medical imaging. Among the most sophisticated is the Large Hadron Collider (LHC) at CERN, which accelerates charged particles to relativistic velocities within a 27-kilometer circular tunnel using a series of radiofrequency cavities and superconducting magnets. The LHC achieves acceleration gradients on the order of $\mathrm{MV{\cdot}m^{-1}}$, with particles traversing the ring multiple times to reach energies in the TeV range [1]. However, the size, cost, and infrastructure required for such facilities limit their accessibility and scalability.

In response, alternative acceleration methods have been developed to provide high-gradient acceleration in more compact geometries. Laser wakefield acceleration is one such technique, leveraging the ponderomotive force of an intense, ultrashort laser pulse propagating through plasma to generate accelerating electric fields exceeding 100 $\mathrm{GV{\cdot}m^{-1}}$—orders of magnitude greater than those attainable in conventional radiofrequency accelerators. These fields enable rapid energy gain over centimeter-scale distances.

Colorado State University (CSU) operates a LWFA platform and is actively engaged in experimental upgrades aimed at increasing beam energy and repetition rate. While LWFA offers exciting prospects for applications ranging from compact light sources to hadron therapy, it also presents new challenges in radiation protection. Electrons accelerated to GeV-scale energies produce highly energetic secondary particles upon interacting with beamline components or diagnostic targets. The resulting radiation fields can pose significant hazards to personnel and equipment if not properly mitigated.

To ensure compliance with radiological safety standards and to implement effective engineering controls (e.g., shielding, exclusion zones), it is essential to characterize these radiation fields quantitatively. Unlike conventional accelerators, the unique source characteristics of LWFA complicate analytical dose estimation. Moreover, the diversity of experimental setups across laboratories hinders standardization of dose assessment procedures [2].

This thesis focuses on the computational characterization of radiation fields generated in LWFA experiments using the Monte Carlo N-Particle transport code. By simulating high-energy electron interactions with target materials and beamline geometries, the spatial, spectral, and angular distributions of secondary radiation can be quantified. These data serve as the foundation for estimating dose rates under various experimental conditions.

1.1.1 Historical Overview

Over the last century, particle acceleration has become an invaluable tool allowing scientists to study the behavior of subatomic particles, yielding monumental discoveries and fundamentally altering our understanding of the interactions that give rise to our macroscopic experience. The first successful particle accelerator was built in 1930, named the Cockroft-Walton generator, which used high voltages to accelerate protons through a potential difference. This was quickly succeeded in 1931 by Ernest Lawrence with his invention of the cyclotron, which became the foundational tool in the study of nuclear physics [3]. In the decades since, particle accelerators have become extremely sophisticated, allowing particles to reach unfathomable energies by the standards of the 20^{th} century.

1.1.2 Laser Wakefield Acceleration

Laser wakefield accelerators are systems utilizing ultra-intense, ultra-short laser pulses to accelerate charged particles, often electrons, within a plasma. This method was first proposed by Toshiki Tajima and John M. Dawson in their seminal 1979 paper [4], and represents the cutting-edge of accelerator physics due to the superior acceleration gradients produced in comparison to traditional accelerators. First, the laser pulse ionizes a gas, producing a plasma, where electrons are free to

move while the heavy cations left behind remain approximately stationary. As the electromagnetic wave packet propagates through the plasma, its electric field pushes electrons outward, leaving a positively charged region in its trail. An electrostatic restoring force causes displaced electrons to oscillate back, forming plasma waves of alternating high and low-density regions. Injected electrons are trapped in the wakefield, gaining energy from the oscillating longitudinal electric field. Electrons leave the acceleration phase when the wakefield becomes sufficiently weak, or when the electrons outrun the wakefield. The final energy of accelerated electrons is dependent upon laser parameters, plasma density, and electron injection conditions. At Colorado State University, electron bundles have demonstrated acceleration gradients as high as 25 GeV $\cdot$ m^{-1} and accelerated electron energies have reliably exceeded 5 GeV [5].

1.1.3 Applications at Colorado State University

Colorado State University is actively advancing LWFA research through its Laboratory for Advanced Lasers and Extreme Photonics (L-ALEPH) and the forthcoming Advanced Technology Lasers for Applications and Science (ATLAS) facility, a $150 million initiative in partnership with Marvel Fusion and the U.S. Department of Energy [6, 7]. At CSU, LWFA is being investigated as a next-generation driver for high-energy electron beams, with applications in compact x-ray free-electron lasers (XFELs). These light sources hold promise for enabling advanced diagnostics in materials science, ultrafast chemistry, and structural biology—fields traditionally reliant on large-scale synchrotron facilities.

Another area of interest is the potential for LWFA to power radiation sources for medical applications. Compact electron and bremsstrahlung sources could support the development of portable or lower-cost radiation therapy systems. This is especially relevant for image-guided radiation therapy and electron-based modalities in oncology.

CSU's research also explores the use of LWFA-generated electrons and secondary emissions, including high-energy photons and neutrons, for applications in nuclear security and nonprolifer-

ation. These particle beams could serve in active interrogation systems or be applied in nuclear diagnostics for inertial confinement fusion experiments [7].

Beyond near-term applications, CSU's collaborations with national laboratories and international partners contribute to long-term goals in high-energy physics. Hybrid acceleration concepts, such as those discussed by the advanced wakefield experiment (AWAKE) collaboration at CERN, are being investigated for future collider designs that combine plasma-based stages with traditional accelerator infrastructure [8, 9].

As these initiatives progress, CSU continues to establish itself as a leading center in the global effort to harness LWFA for both fundamental science and practical applications.

1.2 Radiation and Particle Interactions

Radiation refers to transmission of energy through space or matter in the form of waves or particles. These packets (waves or particles) of localized energy carry intrinsic properties like mass, electric charge, and spin. As radiation travels through media, it can interact with atoms, depositing energy. The mechanism of interaction depends on the radiations characteristics, primarily its mass and electric charge. Particle interactions in matter are inherently probabilistic, governed by interaction cross-sections that quantify the likelihood of various processes—such as scattering, absorption, or nuclear reactions—as a particle travels through a material. Despite the term "cross-section," this measure is not a literal geometric area but a statistical representation of interaction probability, typically expressed in units of area, e.g. barns 10^{-24}cm^2.

In quantum physics, particles exhibit both wave-like and particle-like behavior, allowing them to interact without direct contact. Many interactions are mediated by fundamental forces—like the electromagnetic or strong nuclear force—and can occur over distances much larger than the particle's physical size. As a result, interaction cross-sections can differ significantly from any intuitive "size" of the particles involved, reflecting the complexity of quantum fields and interaction mechanisms rather than just spatial overlap.

1.2.1 Electron Interactions

Electrons, due to their low mass and electric charge, undergo a range of interactions that include both radiative and collisional processes. These interactions govern how electrons lose energy and generate secondary radiation, which in turn shapes the radiological environment in high-energy accelerator systems. The dominant processes include bremsstrahlung radiation, ionization and excitation, elastic scattering, and, indirectly, photon-induced processes such as pair production.

Bremsstrahlung Radiation

Bremsstrahlung, or braking radiation, arises when charged particles—typically electrons—are accelerated while traversing matter. Most commonly, this occurs when electrons are slowed down or deflected by the Coulomb fields of atomic nuclei. The resulting change in velocity leads to the emission of photons, which carry away a portion of the electron's kinetic energy.

While bremsstrahlung is often associated with deceleration, the underlying principle applies to any acceleration, including when electrons gain energy—for example, under the influence of an external electric field. In such cases, the work done by the field increases the electron's kinetic energy, and a small portion of that energy is radiated. This radiation arises because an accelerating charge produces a time-varying electric field, which induces a time-varying magnetic field, resulting in the propagation of electromagnetic waves via Maxwell's equations.

The probability of bremsstrahlung emission increases with both the incident electron energy and the atomic number, Z, of the target material. Consequently, high-Z targets, such as tungsten, are commonly used to generate intense photon fields in accelerator environments. Figure 1.1 illustrates the process of bremsstrahlung emission as an electron undergoes radiative interactions with an atomic nucleus.

Bremsstrahlung energy spectra are continuous with a strong energy dependency, with emission energies extending from near-zero to the kinetic energy of the incident electron. Their angular spectra are also energy-dependent: at low energies, the radiation is roughly isotropic, while at high energies (hundreds of MeV and above), emission becomes strongly forward-directed, confined to a narrow cone along the electron's trajectory [10].

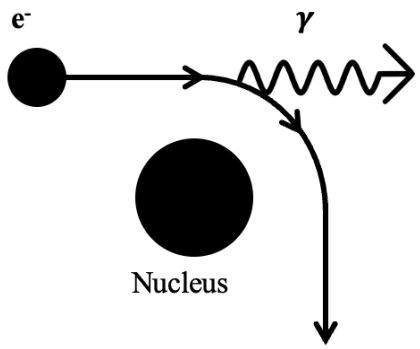

Figure 1.1: Diagram illustrating the process of bremsstrahlung emission by an electron interacting with an atomic nucleus.

Collisional Losses and Delta-Ray Production

Inelastic collisions between fast electrons and atomically bound electrons lead to ionization and excitation. These processes dominate the stopping power of electrons at low to moderate energies and are characterized by the collisional stopping power, which describes the rate of energy loss per unit path length due to electronic interactions.

When an electron with sufficiently high energy transfers a large amount of energy to a bound electron, the latter may be ejected with sufficient kinetic energy to itself become a secondary, trackable particle. These ejected electrons are called delta-rays or δ-rays. Like their parent electrons, δ-rays can further ionize atoms and emit bremsstrahlung radiation, contributing to the complexity of secondary radiation fields in high-energy environments [10]. δ-ray production generally occurs at very low energies (< 1 MeV) and their production is omitted from this work because their relative dose contribution is expected to be very low compared to the dose contributions of high energy photons.

Elastic Scattering and Angular Broadening

Electrons can also scatter elastically from nuclei or atomic electrons without significant energy loss. While individual elastic scattering events only cause small angular deviations, the cumulative effect leads to multiple Coulomb scattering, which broadens the angular distribution of an electron

beam. This process is particularly important when modeling beam transport through high-Z media, as it can impact the spatial distribution of both primary and secondary radiation.

Radiative vs. Collisional Energy Loss

The relative importance of radiative and collisional losses depends on both the energy of the incident electron and the atomic number Z of the target material. Equation 1.1 provides an approximate formula for the ratio of radiative to collisional stopping power, with energy measured in MeV [10].

$$\frac{(-dE/dx)_{\text{rad.}}}{(-dE/dx)_{\text{col.}}} \simeq \frac{Z \cdot E}{800\ \text{MeV}}. \tag{1.1}$$

For tungsten ($Z = 74$), this ratio is unity when the electron's kinetic energy is 10.8 MeV. Beyond this energy, radiative processes begin to dominate.

1.2.2 Photon and Neutron Interactions

Neutron radiation is produced by the interaction of high-energy secondary photons in target and shielding materials. Some relevant neutron production mechanisms and photon interaction mechanisms are discussed in this section.

Once produced, bremsstrahlung photons and secondary neutrons interact with matter via distinct mechanisms. Unlike charged particles, photons and neutrons are uncharged and do not continuously lose energy through electromagnetic field interactions. Instead, they travel in straight paths between discrete stochastic interactions such as photoelectric absorption, Compton scattering, pair production (for photons), or elastic and inelastic scattering (for neutrons). The likelihood of these interactions depends strongly on both the particle energy and the atomic composition of the material. As a result, neutral particles exhibit comparatively long, energy-dependent mean free paths and interact probabilistically rather than continuously along their trajectories.

Pair Production and Annihilation

When a photon with energy exceeding 1.022 MeV, twice the electron rest energy, passes near an atomic nucleus, it may undergo pair production, converting its energy into an electron-positron

pair. This process is forbidden in a vacuum, for momentum conservation could not be achieved by the e^- e^+ pair alone. Some momentum must be absorbed by a recoil nucleus with:

$$\gamma + A \rightarrow e^- + e^+ + X. \tag{1.2}$$

The change in momentum for the recoil nucleus X is negligible and most of the photon energy is contained in the momentum of the particle-antiparticle pair. As with bremsstrahlung emission, pair production increases in likelihood with increasing photon energy and increasing Z of the target material. The inverse of this process occurs when a positron and electron annihilate. In accordance with momentum conservation, two photons with energy $\geq$ 511 keV are produced, traveling in opposite directions

$$e^- + e^+ \rightarrow 2\gamma. \tag{1.3}$$

The 511 keV photons impart a distinctive signature easily observable by most radiation detection systems.

Photonuclear Interactions

High-energy photons may also interact directly with atomic nuclei through photonuclear reactions, leading to nucleon emission. The photon energy must exceed the binding energy of the ejected neutron or proton, generally on the order of several MeV. In general, (γ, n) reactions have lower threshold energies than (γ, p) reactions due to the repulsive Coulomb barrier affecting protons [10]. Generally, the probability of photonuclear interaction is significantly lower than the combined probabilities of other photon interactions, although some materials like berylium have relatively low thresholds. Ihe introduction of neutron radiation necessarily imposes special protection considerations [11]. These interactions are important contributors to secondary neutron production in high-energy environments and must be considered in shielding and dose assessments.

Exotic Radiation Production

At photon energies far exceeding those required for electron-positron pair production, heavier particle pairs can be generated. In particular, high-energy photons may produce muon $(\pm)$ pairs in the electromagnetic field of a nucleus. This quasi-elastic process is described by:

$$\gamma + A \rightarrow \mu^+ + \mu^- + X, \tag{1.4}$$

where A denotes the mass number of the nucleus and X indicates a potentially excited or fragmented nuclear state. The threshold for this process occurs at photon energies exceeding $2m_\mu \approx 211$ MeV. Exploratory studies of this mechanism have been discussed in the context of high-intensity muon sources, such as the Gamma Factory project [12]. Muons may also be generated indirectly through the photoproduction of pions. In this process, a high-energy photon interacts with a nucleon in the nucleus to generate charged pions:

$$\gamma + p \rightarrow \pi^+ + n, \tag{1.5}$$

$$\gamma + n \rightarrow \pi^- + p. \tag{1.6}$$

followed by the pion's decay. The most probably decay schemes for charged pions are:

$$\pi^+ \rightarrow \mu^+ + \nu_\mu. \tag{1.7}$$

$$\pi^- \rightarrow \mu^- + \bar{\nu}_\mu. \tag{1.8}$$

The products of exotic particle decay and their mean lifetimes [13] are provided in Table 1.1.

Neutron Interactions

Neutrons interact with matter via nuclear reactions that depend heavily on their kinetic energy. Unlike charged particles, neutrons are electrically neutral and can travel significant distances before interacting, making them particularly penetrating and challenging from a radiation protection

Table 1.1: Decay characteristics of select mesons and leptons.

Particle	Decay Products	Decay Time
π^+	$\mu^+ + \nu_\mu$	26.03 ns
π^-	$\mu^- + \bar{\nu}_\mu$	26.03 ns
π^0	2γ	8.4×10^{-17} s
μ^+	$e^+ + \nu_e + \bar{\nu}_\mu$	2.197 μs
μ^-	$e^- + \bar{\nu}_e + \nu_\mu$	2.197 μs

perspective. After their production—typically with high (MeV-scale) kinetic energies—neutrons undergo a process of moderation, progressively losing energy through successive scattering events until they are either absorbed or reach thermal equilibrium with the surrounding medium.

Neutrons are commonly categorized by energy into distinct regimes, each associated with characteristic interaction mechanisms:

Thermal neutrons, with energies around 0.025 eV at room temperature, predominantly undergo radiative capture reactions (e.g., (n, γ)). The probability of these interactions typically follows a $1/v$ dependence, where v is the neutron velocity, leading to high cross sections at low energies. Capture may yield prompt gamma emission, charged particles, or even lead to nuclear activation. For example, thermal capture on cobalt or copper can result in the production of long-lived radionuclides such as ^{60}Co or ^{64}Cu, both of radiological concern.

Epithermal and resonance neutrons, spanning energies from roughly 1 eV to 100 keV, interact in a regime where nuclear cross sections exhibit sharp fluctuations known as resonance peaks. These arise from quantized energy levels in the compound nucleus formed during the reaction and can significantly enhance absorption probabilities in certain isotopes. Resonance absorption is particularly relevant in materials like uranium, tungsten, or iron, and plays a key role in reactor physics and shielding design.

Fast neutrons, with energies in the hundreds of keV to tens of MeV, primarily undergo elastic and inelastic scattering with nuclei. These interactions can transfer substantial kinetic energy to target nuclei, producing high-LET (linear energy transfer) recoil particles that contribute significantly to dose in tissue. Additionally, fast neutrons can induce nuclear

reactions such as (n, p), (n, α), $(n, 2n)$, and in fissile materials, (n, f) fission reactions. These reactions may emit secondary particles including protons, alpha particles, secondary neutrons, and prompt gammas. Fission, while not a dominant process in most laser wakefield scenarios, is nonetheless important for certain shielding assessments and materials exposed to high-fluence neutron fields.

Throughout this slowing-down and interaction chain, neutrons contribute to both prompt and delayed radiation fields. Secondary gamma rays, activation products, and recoil nuclei all factor into shielding calculations and dose estimation. For example, iron commonly used in structural concrete can become activated, producing radionuclides such as ^{55}Fe, although more significant sources of activation (e.g., ^{60}Co from cobalt impurities) often dominate long-term radiological concern.

The interactions of secondary photons and neutrons are central to understanding radiation protection issues around high-energy accelerators. As such, accurate characterization of these interactions is critical in the Monte Carlo modeling of transport and shielding scenarios associated with laser wakefield accelerator systems.

1.3 Dose and Radiation Protection Considerations

1.3.1 Definition of Radiation Dose

Radiation dose quantifies the energy imparted by ionizing radiation to matter, and in the context of radiological protection, to biological tissue. The fundamental quantity is the *absorbed dose* D, defined as the mean energy deposited per unit mass:

$$D = \frac{\mathrm{d}\bar{\mathcal{E}}}{\mathrm{d}m}, \quad \text{[Gy = J/kg]}, \tag{1.9}$$

where $\mathrm{d}\bar{\mathcal{E}}$ is the mean energy deposited in mass $\mathrm{d}m$ of tissue or detector material. While absorbed dose is the foundation of dosimetry, it does not account for the differing biological effects of various radiation types.

To address this, the concept of *equivalent dose* H is introduced, incorporating a radiation weighting factor w_R that accounts for the type and energy of the radiation:

$$H = \sum_R D_R \cdot w_R. \tag{1.10}$$

Here, D_R is the absorbed dose from radiation type R. For photons electrons and muons, $w_R = 1$, while for other forms of radiation, w_R can range significantly higher due to their greater biological effectiveness. For protons and charged pions, $w_R = 2$, for alpha particles, $w_R = 20$, and for neutrons, w_R is a function of the neutron energy. Figure 1.2 shows the functional dependency between the radiation weighting factor and neutron energy outlined in the 2007 recommendations of the ICRP [14].

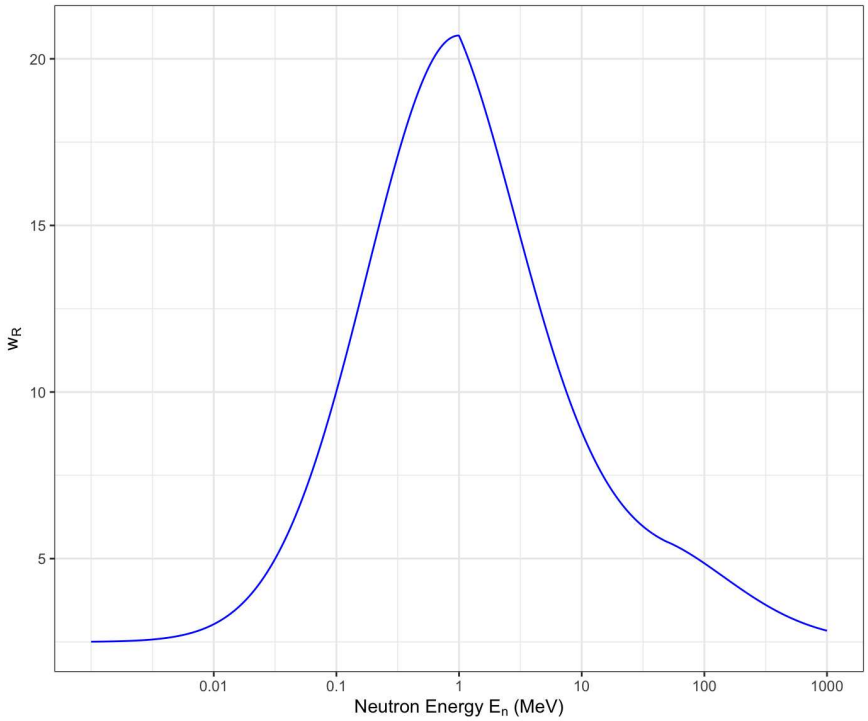

Figure 1.2: Plot of neutron radiation weighting factors vs. energy.

The *effective dose* E further considers the varying sensitivities of different tissues to stochastic radiation effects by applying tissue weighting factors w_T:

$$E = \sum_T w_T \cdot H_T = \sum_T w_T \sum_R w_R \cdot D_{T,R}. \tag{1.11}$$

Effective dose, expressed in sieverts (Sv), is the principal quantity used in radiation protection to estimate overall risk to human health from external and internal exposures by the 2007 international reccomendations on radiological protection [14].

1.3.2 Dosimetric Considerations for LWFA Facilities

Laser wakefield accelerator systems present unique dosimetric challenges due to their production of ultra-short, high-energy bursts of radiation. These fields are often highly directional and pulsed, with significant contributions from bremsstrahlung photons and secondary neutrons. Key considerations include:

Pulsed radiation fields: Standard survey instruments may under-respond or saturate due to the extreme instantaneous dose rates. Specialized detectors with high temporal resolution or integrating capabilities may be necessary [15].

Spectral complexity: LWFA sources produce broad energy spectra, especially for photons, ranging from keV to multiple GeV. Neutrons may span thermal to high-energy regimes. Dose calculations must be spectrally resolved and account for fluence-to-dose conversion coefficients across this range [16].

Directional fields: Strong anisotropy in photon and neutron emission complicates placement and interpretation of dosimeters and necessitates angularly resolved measurements or simulations.

Computational dosimetry: Monte Carlo methods, such as MCNP, are essential to model complex geometries and spectra. These tools compute particle fluence distributions and can translate them to dose in various ways such as using ICRP-based conversion coefficients.

Shielding and occupancy modeling: Physical dosimetry alone may not be sufficient for safety evaluation. Shielding calculations and access control modeling are critical for ensuring compliance with occupational dose limits.

1.3.3 Calibration and Instrumentation Challenges

High-energy, mixed-field environments pose significant difficulties for dosimeter calibration. Some pertinent calibration considerations include:

Lack of calibration standards: Most dosimeters are calibrated using reference fields of known energy and composition (e.g., ^{137}Cs, ^{60}Co, AmBe). These may not be representative of the ultra-relativistic spectra in LWFA environments, leading to significant response errors [15].

Energy-dependent detector response: Instruments such as ionization chambers, TLDs, and solid-state detectors may over- or under-respond depending on the incident particle spectrum and angle.

Environmental factors: Secondary particle production in nearby structures (walls, beamline components) may further alter the radiation field, necessitating in-situ characterization or corrections based on detailed simulations [10].

To overcome these challenges, facilities often rely on a combination of direct measurements, simulation-based corrections, and conservative estimates for radiation field characterization and worker dose assessment.

1.3.4 Photon vs. Neutron Dosimetry

Photons and neutrons differ fundamentally in their interaction mechanisms and dosimetric characteristics.

Photon dosimetry is well established, supported by standardized instrumentation and conversion coefficients. Photons deposit energy primarily through the photoelectric effect, Compton

scattering, and pair production. These interactions transfer energy to charged particles—typically electrons—which then lose energy continuously via ionization and excitation of atoms in tissue-equivalent media, resulting in localized dose deposition [17]. Neutron dosimetry, in contrast, is much more complex. Neutrons interact indirectly, primarily through elastic scattering and nuclear reactions. Their biological effect per unit fluence is highly energy-dependent, leading to large variations in dose conversion coefficients—up to two orders of magnitude between thermal and fast neutrons [16].

Detector technologies differ as well: photons are commonly measured using ionization chambers, scintillators, and semiconductor detectors, while neutron dosimetry often requires proportional counters, moderated detectors, or activation foils [15]. Some hybrid detectors attempt to discriminate neutron and photon contributions in mixed fields, but such methods require careful calibration.

Given the high-energy environment of LWFA systems and the presence of both photon and neutron fields, accurate dose assessment requires a multimodal approach—integrating physical measurements, particle transport simulations, and knowledge of source geometry and spectra. Emphasis should be placed on neutron dosimetry due to the potentially higher dose per unit fluence and the relative scarcity of well-characterized detector responses at high neutron energies.

1.4 Monte Carlo N-Particle Transport Code

Particle transport simulations are typically performed using either deterministic or Monte Carlo methods. Both approaches are based on the Boltzmann transport equation, which describes the distribution of particles—such as neutrons, photons, or electrons—as they travel through and interact with matter. In radiation transport simulations, this equation accounts for all processes that can change the particle distribution at a given location, including particle scattering, absorption, and production. Deterministic methods solve the equation directly using numerical techniques on a discretized mesh, while Monte Carlo methods, as implemented in MCNP, estimate solutions statistically by simulating the random trajectories of many individual particles. Each interaction of a

particle's lifetime is sampled using pseudo-random numbers. Upon calculating the lives of many particles, the tally results are averaged to infer physical quantities like flux or dose with statistical confidence [13].

1.4.1 Overview and Capabilities

The Monte Carlo N-Particle transport code, developed by Los Alamos National Laboratory, models transport and interactions of 37 types of particles spanning a wide range of energies through a user-specified geometry. This thesis employs the latest versions of the code, 6.2 and 6.3, for investigation of particle production and dose rate estimation resulting from high energy electrons originating in laser wakefield acceleration experiments. The objective of any MCNP simulation is to provide measurements of physical quantities which are calculated through seven user-specified standard tallies. Tallies record information about particles as they pass through or interact with specific regions in the problem geometry, effectively acting as detectors. Tallies can measure quantities such as fluence, energy deposition, and dose. Naturally, certain tallies are better suited to particular problems than others. Table 1.2 provides brief descriptions of the standard tallies available in MCNP. A thorough description of MCNP tallies is found in section 2.5 of the MCNP user manual [13].

Table 1.2: Standard tallies available in MCNP

Tally	Description	Units
F1	Surface Current	particles
F2	Fluence Through Surface	particles cm^{-2}
F4	Fluence Through Volume	particles cm^{-2}
F5	Fluence Near a Point	particles cm^{-2}
F6	Energy Deposition	MeV g^{-1}
F7	Fission-Energy Deposition	MeV g^{-1}
F8	Pulse-Height	pulses

MCNP normalizes all tally measurements to the number of histories, a tally measuring particle fluence is thus a statement of the average fluence per source particle.

1.4.2 Electron Transport in MCNP

Previous iterations of MCNP are notorious for having difficulties with charged particle transport, particularly with respect to electron transport. Due to the electrons low mass, most of its interactions are electromagnetic in nature. As a result, monte-carlo calculations for electron transport require a dramatic increase in substeps compared to neutral and heavy charged radiation, and in turn, yield a similar increase in computational burden for each electron transported. This computational demand is further compounded at energies beyond cross-section thresholds.

MCNP 6 introduced extensive efforts to improve the reliability of electron transport with notable advancements to high-energy simulations. MCNP has refined its treatment of elastic scattering, particularly at high electron energies where the scattering angle becomes strongly forward-peaked, leading to increasingly accurate simulations of electron trajectories at high energies [18]. MCNP 6.2 rolled out the introduction of δ-ray production available in the electron physics card. This feature exponentially increases the number of electrons generated, enhancing the accuracy or energy deposition calculations and simultaneously increasing computational demand [19].The single-event method for electron transport is a notable addition that models individual electron interactions without relying on multiple-event scattering approximations. The transition to a single-event method provides a substantial advancement in transport capability for electrons and photons. This method is especially beneficial at low energies and has potential applications at higher energies pending further validation [20].

These improvements hardly scratch the surface of the litany of improvements implemented since the release of version 6.0. Despite these advancements, certain limitations persist. The single-event method for example, while far more accurate, requires significantly more computational resources, limiting practicality for extensive simulations. Generally, while the recent additions actively serve to improve the accuracy of electron transport, they necessarily increase MCNP's computational demand dramatically. Furthermore, there is evidence suggesting that further validation and refinement may be required for problems involving electron transport at higher energies [21].

1.5 Project Goals

The primary objective of this thesis is to develop and validate MCNP simulation models that characterize the radiation environment associated with LWFA conducted in the Advanced Beam Laboratory (ABL 103) at Colorado State University. LWFA offers a compact means of accelerating electrons to relativistic energies over short distances, but the ultrashort, high-intensity laser pulses and resulting electron beams generate significant prompt radiation, including bremsstrahlung photons, secondary neutrons, and other high-energy particles.

This study seeks to:

- Construct geometry-specific MCNP models that replicate key features of the experimental setup in ABL 103.
- Provide source definitions and data products that can be used in secondary transport simulations for shielding optimization and facility safety assessments.
- Quantify the radiation field produced by monoenergetic electron beams incident on high-Z converter materials, focusing on the spectral, angular, and spatial distributions of emitted photons and neutrons.
- Calculate effective dose with energy-dependent conversion coefficients (E/Φ) to estimate the effective dose delivered per primary accelerated electron operating conditions.

Ultimately, this work aims to support radiation protection efforts and facilitate safe operational protocols for future high-power LWFA experiments at CSU. By characterizing dose-relevant radiation outputs at their origin, the models developed herein will contribute toward a predictive framework for accelerator radiation safety, tailored to the unique parameters of laser-driven electron acceleration.

Chapter 2

Methodology

2.1 Methodology Overview

This study employs a multi-stage computational workflow designed to simulate particle transport and estimate radiation dose rates around an LWFA environment. The methodology is organized into four primary steps:

1. **Secondary photon generation.** A simplified geometry model is used in MCNP to simulate the interaction of a monoenergetic electron beam with a high-Z target. The resulting bremsstrahlung photon emission is tallied using surface flux tallies (F2) to extract energy- and angle-resolved spectra.

2. **Photon source definition.** The energy and angular fluence distributions obtained from MCNP are processed using the R statistical environment. These data are used to construct a tabular photon source definition (via SDEF and associated SI/SP distributions), representing a physically accurate input for secondary transport simulations.

3. **Dose estimation in detailed geometry.** A high-fidelity model of the accelerator environment is constructed in MCNP, incorporating structural and shielding components. The previously defined photon source is used to simulate transport through this geometry. Dose rates at various locations are estimated using point detector tallies (F5).

4. **Post-processing and visualization.** F5 tally outputs are parsed and analyzed in R to generate dose rate maps, evaluate dose contributions by energy and particle type, and visualize spatial distributions of radiation fields in operationally relevant regions.

This workflow enables decoupling of primary electron transport from secondary radiation field modeling, facilitating dose rate estimation around the LWFA facility at CSU.

2.2 MCNP Simulation Setup

The MCNP simulation geometry is based on Room 103 of the Advanced Beam Lab (ABL 103) at Colorado State University. ABL 103 is approximately 24.7 meters long and 10.2 meters wide and houses equipment for a variety of experiments. A diagram of the simulated geometry is provided in Figure 2.6. The wakefield experimental setup occupies roughly one-third of the lab space, with the laser apparatus located near the center of the room and instrumentation distributed in multiple directions for concurrent experiments. The wakefield electron beam is directed toward the northeast corner of the room.

2.2.1 MCNP Geometry and Materials

The beamline includes a small tungsten target, measuring 2 in $\times$ 2 in $\times$ 4 in, followed by an aluminum collimator used to steer charged particles toward a beam-stop assembly. The MCNP geometry explicitly includes the aluminum box to account for potential scattering effects, magnetic fields are excluded from the model.

The materials defined for the simulations are composed according to the Pacific Northwest National Laboratory compendium of material composition data [22], which provides isotopic compositions. Due to the high energies, many interactions of interest depend on isotopic compositions, determined using the National Institute of Standards and Technology (NIST) material composition database [23]. The beam-stop consists of a small air cavity, surrounded by a lead shell designed to attenuate and absorb radiation. The back of the lead shell is approximately 10 cm thick, while the lateral thicknesses are approximately 5 cm. The lead is further encased in a non-borated polyethylene layer which provides additional attenuation for charged particles and moderates fast neutrons. The floor is made of concrete and the walls and ceiling are gypsum. A summary of materials, densities, mass-fractions, and isotopic compositions is presented in Table A.1.

The electron source is a point source located at the origin of the coordinate system, emitting particles along the positive y-axis. The electron source is run in a simplified version of the geom-

etry, described in Section 2.3.2. Figure 2.1 provides top and side views of the MCNP geometry, including zoomed-in perspectives of the beamline assembly.

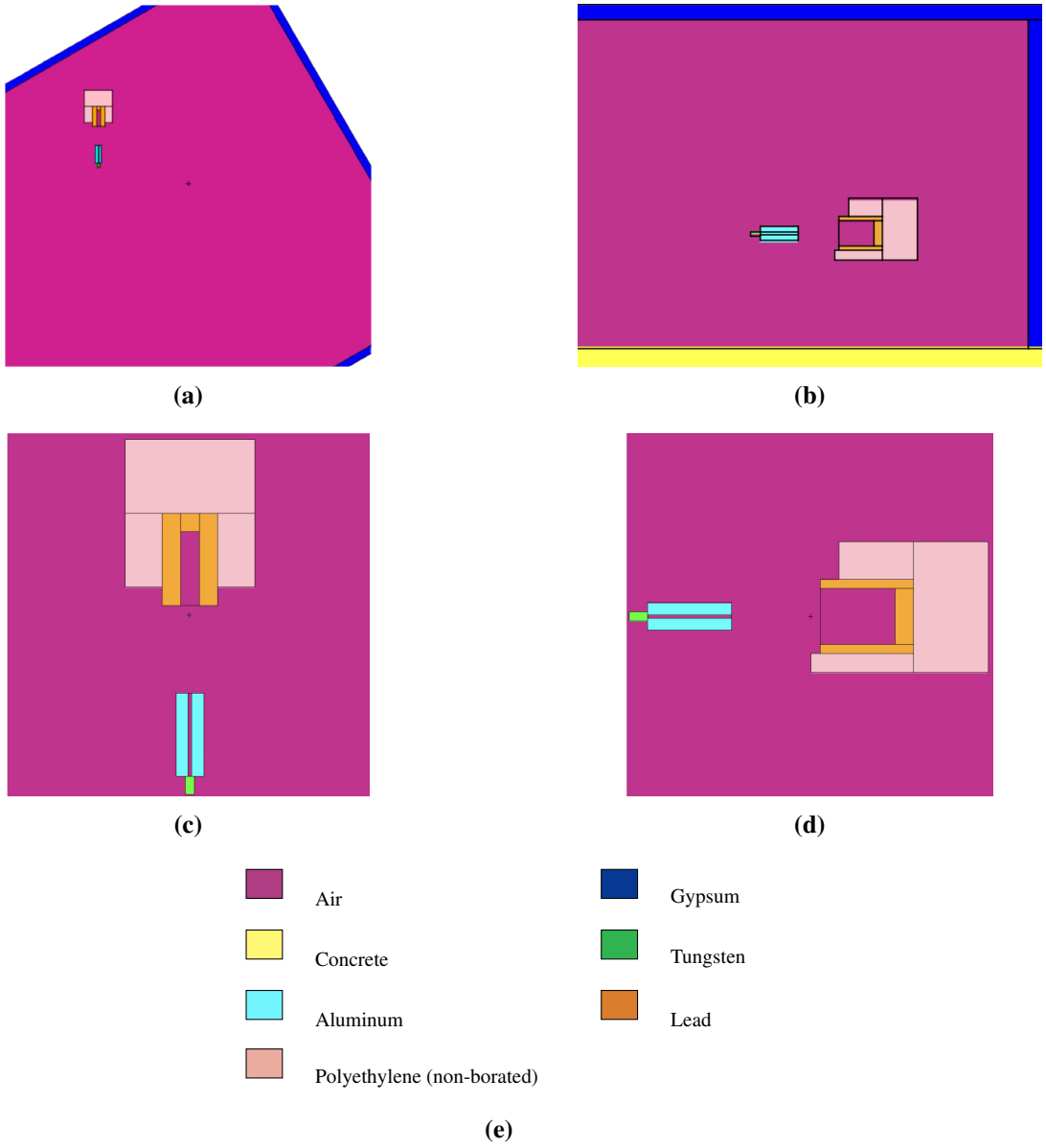

Figure 2.1: MCNP geometry as seen from two perspectives, colored by material type. (a) Top-down full view (xy-plane). (b) Side full view (yz-plane). (c) Zoomed top-down view. (d) Zoomed side view. (e) Material color legend.

2.2.2 Interaction Data

The library identifiers specified in the materials cards govern MCNP's treatment of particle interactions through tabulated interaction cross-section data. Each library identifier references a particular, particle-specific class of interactions and provides MCNP with interaction probabilities to use in its calculations as it transports particles through materials. These data are user-selected on a case-by-case basis and depend on the type of problem. Interaction cross-section evaluations available for MCNP come from a multitude of libraries. Data exists for various modes of particle interaction and data selection depends heavily upon the problem.

At extreme energies, electrons have the capacity to produce many forms of secondary radiation which undergo their own interactions. The predominant interactions of concern for these simulations are nuclear and photonuclear. While only one library exists for electron data, there are many libraries available for nuclear and photonuclear interactions. These data are differentiated through properties including temperature and energy limits. Selection is largely dependent upon these properties, although it is good practice to select data from more recent evaluations when possible.

The interaction libraries used in this work are selected for their upper energy limits and temperature, generally around 300 K. Nuclear data are all continuous-energy. The tables selected for nuclear and photonuclear interactions and relevant information pertaining to these tables are found in Tables A.2 and A.3 [24]. In circumstances where interaction data is not available, physics models are applied.

2.2.3 Physics Models

In problems with particularly high energies, interaction data does not provide MCNP with sufficient information to carry out its calculations. In these cases, physics models are applied. Wakefield electrons regularly obtain energies up to several GeV, however cross-section data have a maximum cutoff energy of 150 MeV, and often the cutoff is much lower, on the order of tens of MeV. The reason for this energy restriction is that beyond 150 MeV, interactions like pion

production begin to dominate, and model physics options are generally better suited for these mechanisms due to a lack of data for these ranges [13].

High-energy physics models have been fine-tuned to suit the wakefield problem, with particular emphasis on bremsstrahlung and photonuclear biasing. Photonuclear biasing causes one photonuclear event to be sampled each time a photoatomic event occurs. This process causes far more neutrons to be produced, each with a lower statistical weight. Each neutron will therefore contribute less to tallies while improving the variance of neutron measurements. Increasing the number of neutrons sampled in this manner is a form of variance reduction. This technique is especially useful for low probability interactions like photonuclear that result in radiation which contributes significantly to dose.

2.2.4 F2 Tallies and Bins

F2 tallies measuring photon surface fluence are applied to quantify the photon distribution generated in a target resulting from an electron beam source. The direction and energy of secondary photons are used to generate probability distributions used to construct a secondary photon source. Selection of energy bins correspond to energies which the International Commission on Radiological Protection (ICRP) have tabulated effective dose per fluence conversion coefficients in publication 116 [16]. These values and their dose per fluence conversion coefficients are provided in Table A.4. For many tally types in MCNP, results can be fine-tuned through the use of bins. There are two bin types relevant to this work: energy bins, which separate tallies by particle energy; and direction bins, which sort data based on the particles angle of incidence relative to a surface normal vector assigned by MCNP. All tallies can be binned by energy, however only the surface tallies, F1 and F2, can be binned by direction [13].

An unbinned tally records the total tally value per source particle in the tallied region. In contrast, a binned tally separates the tally contributions based on the specified bin type(s), providing more detailed information about how the tally value varies with energy, and/or direction. If bins are not specified, tallies will accumulate into a single total bin.

2.2.5 F5 Tallies, and Dose

Measurements of fluence near a point (F5) are applied for photons and neutrons in regions near the beamline. These tallies are used to estimate the effective dose by including data providing the effective dose per unit fluence incident on antero-posterior (AP) geometry for monoenergetic radiation, obtained from ICRP 116 [16]. To fill in the gaps between energies, MCNP applies a logarithmic interpolation. Spline fits of log-interpolated values that have been transformed back is visualized in Figures 2.2- 2.4. Unique behavior is observed for neutron and photon conversion factors. In particular, across the same energies, neutron doses outweigh photon doses by up to an order of magnitude. Point detector tallies are placed near doors and entry vestibules. Fluence values are converted to effective dose with:

$$E_{\text{Eff},R}(\vec{r}) = \Phi_{\text{F}n} \cdot \kappa_R(E) \tag{2.1}$$

where,

$E_{\text{Eff},R}(\vec{r}) =$ total effective dose per starting particle at point $\vec{r}$ from radiation type R,

$\Phi_{\text{F}n} =$ fluence from tally n per starting particle,

$\kappa_R(E) =$ effective dose per fluence of radiation type R with energy E.

Fluences measured at point detectors are converted to dose at a point centered at the detector position. F5 tallies are restricted in that they only allow measurement of photons and neutrons. Electron doses are omitted largely because it is not anticipated that personnell are in the room during experiments and thus electrons will pose a negligible threat.

2.3 Source Specifications

2.3.1 The Piece Wise Approach

Due to the inefficiencies and need for further validation of MCNP's electron transport models discussed in the introduction, a piece wise approach is employed to constructing source defini-

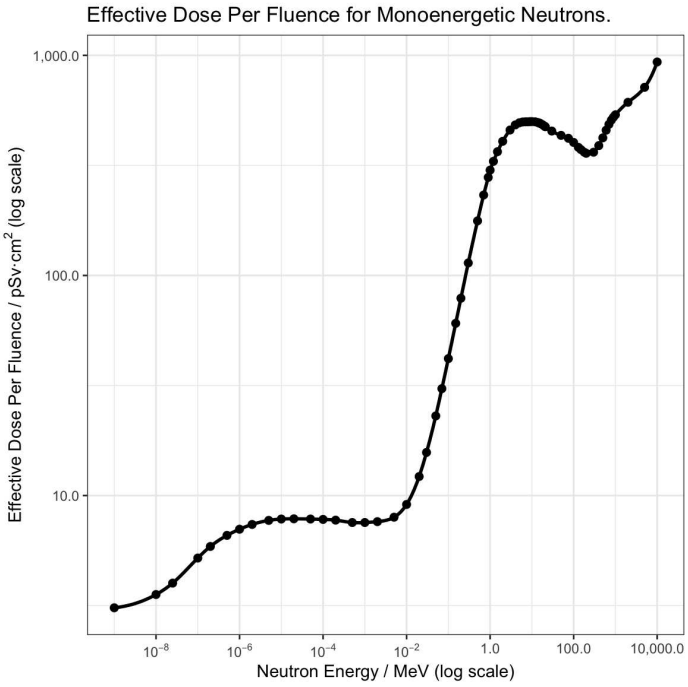

Figure 2.2: Plot of fluence-to-dose conversion data from ICRP 116 for monoenergetic neutrons incident on AP geometry.

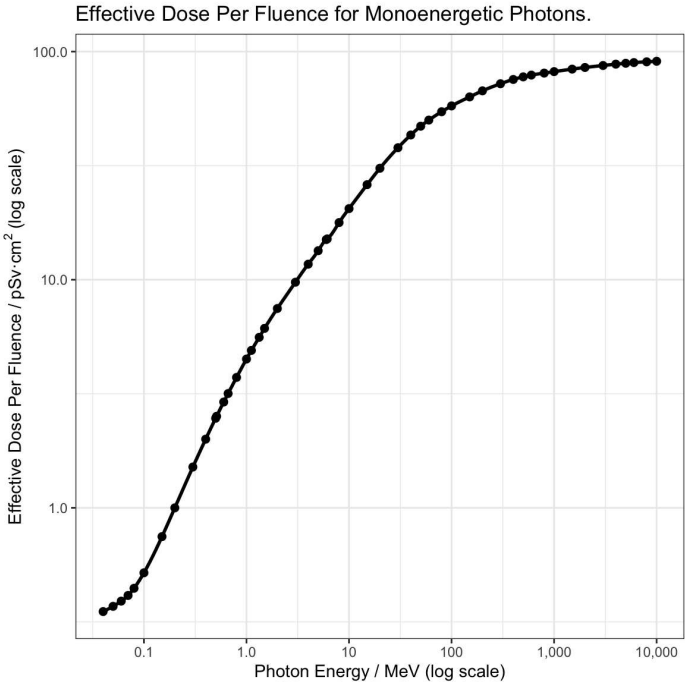

Figure 2.3: Plot of fluence-to-dose conversion data from ICRP 116 for monoenergetic photons incident on AP geometry.

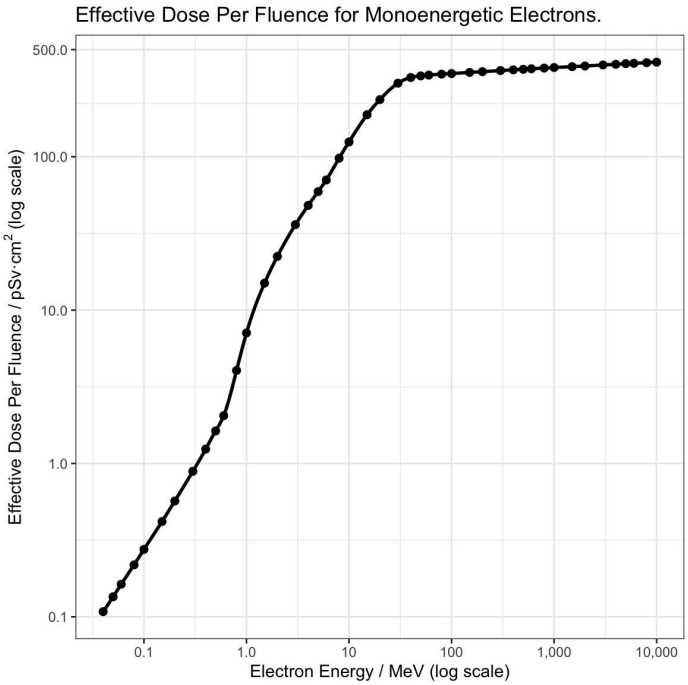

Figure 2.4: Plot of fluence-to-dose conversion data from ICRP 116 for monoenergetic electrons incident on AP geometry.

tions. The initial batch of simulations using an electron source, followed by a secondary batch of simulations employing a photon source, determined by measuring the distributions of photons that result from the initial model results. This technique prevents excessive runtimes by minimizing the requirements placed on the GeV scale electron sources.

2.3.2 Primary Electron Source

The primary particle source, and the basis of the simulation, is a narrow beam of electrons. As electrons enter the tungsten target, creating secondary radiation through interactions discussed in the introduction. Secondary photons will undergo further interactions including photonuclear and pair production, further contributing to dose.

The wakefield facility produces electrons with incident energies of several GeV and is not limited to any particular value or range. At the time of this analysis, electron energies at the Advanced Beam Lab have reached up to 9 GeV. To adequately capture these capabilities, MCNP was run with an electron source at ten energies ranging from 100 MeV to 10 GeV, Equation 2.2

provides the discrete subset of electron energies used in the simulations. The selected energies are all in the typical range for modern wake-field accelerators. The results of this model can be applied to continuous-energy electron spectra with appropriate regression models estimating the number of photons generated.

$$E_{e^-} \in \left\{ \begin{array}{c} 0.1\,\text{GeV},\ 0.15\,\text{GeV},\ 0.2\,\text{GeV},\ 0.5\,\text{GeV},\ 0.7\,\text{GeV}, \\ 1.0\,\text{GeV},\ 3.0\,\text{GeV},\ 5.0\,\text{GeV},\ 7.0\,\text{GeV},\ 10.0\,\text{GeV} \end{array} \right\} \tag{2.2}$$

In the interest of computational efficiency, this source is initiated in a highly simplified geometry. The room is replaced with a void sphere centered at the origin with a radius of 5 m. The only component of the beam line that remains is the tungsten target. Electrons originate at the center of the sphere along the y-axis, toward the target. Such simplification ensured that secondaries are generated only within the target, and the resultant photon distributions are therefore purely representative of photons originating in the target. The simplified geometry is shown in Figure 2.5.

MCNP distinguishes classical particles as electrons, positrons, photons, and neutrons. When transport is turned on for non-classical particles, MCNP will not use parallel processing, dramatically slowing large-history runs. To further improve performance, only electrons, photons, and neutrons are transported. Despite the potential for exotic secondary radiation, particles such as muons and pions have negligible influence on the bremsstrahlung spectra generated by primary source electrons. While they are capable of contributing to dose, their direct impact is expected to be minimal because they generally decay before undergoing substantial interactions with matter. Their short lifetimes limit the distance over which they can deposit energy directly, reducing their dosimetric significance in most scenarios.

The tungsten block acts as the detector, with energy and cosine-binned F2 tallies placed on each surface. These tally results are used to construct the energetic and angular spectra of photons generated in the block. The resultant photon distributions are used to generate the secondary photon source.

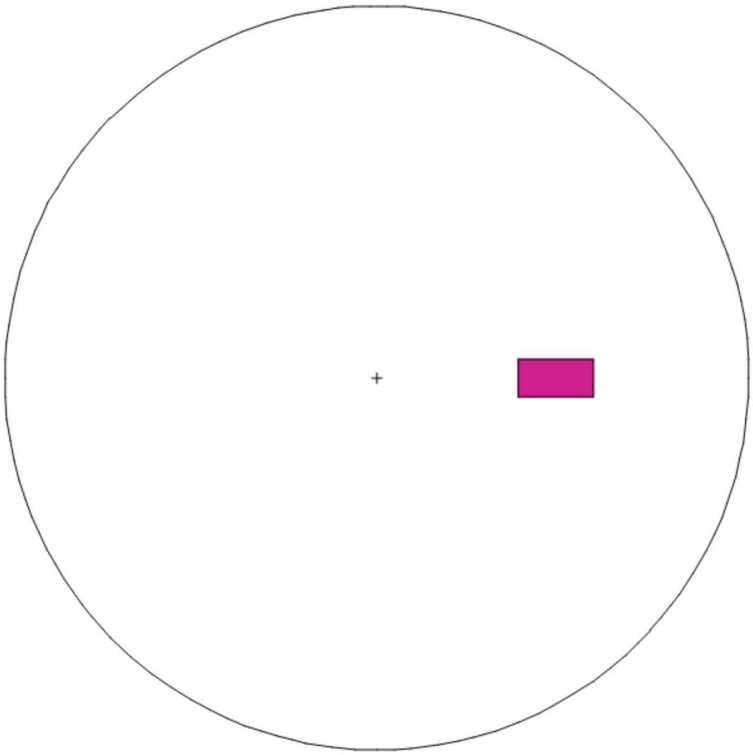

Figure 2.5: Simplified electron source geometry. Electrons are emitted from the center toward the tungsten target, colored magenta.

2.3.3 Secondary Photon Source

The photon source, located in the center of the tungsten block, is substantially more complex than the primary electron source. MCNP first samples an emission direction from a user-specified probability distribution generated from the results of the electron simulation. Once a direction is chosen, the energy of the photon is sampled from a conditional energy distribution specifying the probability of emission energy given an emission direction. The effective dose at a point per starting photon obtained by Equation 2.1 is multiplied by the number of photons generated by a source electron of energy E_{e^-}, providing the effective dose per electron:

$$E_{\text{Eff},R}(\vec{r}; E_{e^-}) = E_{\text{Eff},R}(\vec{r}) \cdot N_\gamma(E_{e^-}). \tag{2.3}$$

Non-classical particle transport and the appropriate physics models are turned on for the photon simulations. While muons will contribute to dose, limitations in the chosen tally methods demand

they not be tallied for the purposes of this work. Furthermore, their incredibly short mean lifetimes cause them to be highly unlikely to significantly contribute to dose. For the same reasons, pions are not tallied either. Although neutrinos are generated in many interaction and decay mechanisms, their likelihood of interaction is sufficiently small that their transport is omitted from these simulations.

As with the dose measurements, multiplying by the appropriate weighting factors from Equation 2.10, provides an estimate for the number of each particle type produced per starting wakefield electron. Figure 2.6 shows the extended simulation geometry bounded by the tallying sphere.

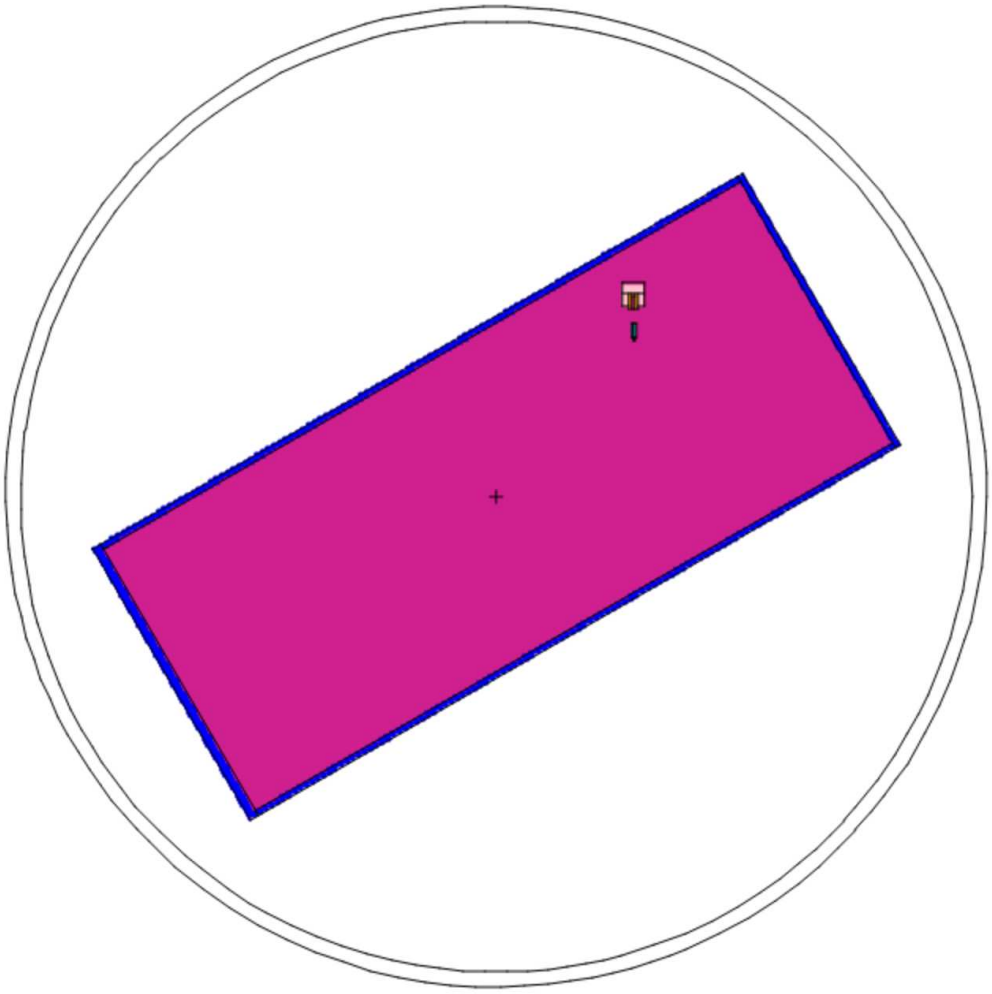

Figure 2.6: Image of the xz-plane, showcasing the full geometry of the photon simulations, including the external tally sphere.

2.4 Data Analysis

2.4.1 Use of Iterated MCNP Runs

When running MCNP, it is often most efficient to use threading, meaning execution of a simulation over many processors. In this regime, many calculations can be executed simultaneously. For problems with exceptionally high energies, MCNP will turn threading off for calculations above data threshold energies. Another extenuating factor damaging efficiency is that threading is forbidden for simulations transporting any particles other than photons, neutrons, and electrons. These threading limitations dramatically increase MCNP's runtime.

Furthermore, a tally with numerous bins will have relative uncertainties for each bin and a total relative uncertainty. While the chosen number of histories may be sufficient to obtain acceptable uncertainty for the total tally, the binned uncertainties may not be so. The relative uncertainty recorded for a cumulative tally is inversely proportional to the square root of the number of histories used in the run, this is not necessarily the case for binned uncertainties. In order to maintain reasonable runtimes and adequate binned statistical results, several iterations of the same simulation are run with unique strings of pseudorandom numbers.

If the sum of the number of histories over all runs is the same as that for a long run, then effectively the same results are obtained in less time. With appropriate uncertainty propagation, statistics between many unique simulations of the same model can be combined, and statistical fidelity for binned results is obtained.

2.4.2 Uncertainty Propagation

Particle fluences measured by MCNP via the F2 tally, $\bar{\Phi}$, are reported as the mean number of particles of a given type crossing a surface, per unit area, per source particle history. Accompanying the fluence is a relative uncertainty (referred to as relative error by MCNP), which corresponds to the standard error of the mean of the measurement:

$$u_r(\bar{\Phi}) = \frac{u(\bar{\Phi})}{\bar{\Phi}}, \tag{2.4}$$

where $u(\bar{\Phi})$ is the standard uncertainty of the mean. Note that MCNP computes this value from the variance of tally contributions across histories; it is not based on a Poisson distribution. For illustration, the standard deviation for a Poisson-distributed count variable is given by

$$u(\bar{\Phi}) = \sqrt{\bar{\Phi}}. \tag{2.5}$$

However, this formula is not used by MCNP for F2 tally uncertainty estimates.

To prevent indeterminate values later in the data processing pipeline and to ensure all measurements are utilized, two special edge cases require substituted uncertainty estimates:

Case 1: No particles cross a tally bin ($\bar{\Phi} = 0$ and $u(\bar{\Phi}) = 0$). Although the measurement is zero, it still carries uncertainty that MCNP does not report. In this case, we conservatively estimate the uncertainty as

$$u(\bar{\Phi}) = \frac{1}{NPS},$$

where NPS is the total number of source particle histories. This value is not arbitrary: it corresponds to the standard deviation (i.e., 1σ upper bound) for a Poisson-distributed variable with zero observed counts, normalized per history. In other words, even if no particles are detected, the upper bound for the true mean is nonzero, and $\frac{1}{NPS}$ reflects the minimum resolvable fluence from a single particle crossing over the course of the simulation. This maintains continuity with low-count statistics and avoids falsely implying perfect knowledge in zero-count bins [15].

Case 2: A nonzero fluence is reported ($\bar{\Phi} \neq 0$), but $u(\bar{\Phi}) = 0$ due to truncation below MCNP's precision limit. In this case, we substitute

$$u(\bar{\Phi}) = 5 \times 10^{-5},$$

which is half the smallest nonzero relative uncertainty MCNP can report. This ensures finite error bars for all tally bins, even those with very low variance, enabling uncertainty propagation to proceed robustly.

All subsequent uncertainty estimates in derived quantities follow the standard uncertainty propagation formula for a function of n independent variables, $f(x_1, x_2, ..., x_n)$, where each x_i has uncertainty $u(x_i)$:

$$u\left(f(x_1, x_2, ..., x_n)\right) = \sqrt{\sum_{i=1}^{n} \left(\frac{\partial f}{\partial x_i}\right)^2 u(x_i)^2}. \tag{2.6}$$

2.4.3 Fluence Combination for Multiple Runs

The initial simulations are structured in such a way that the overall tallies have adequate statistics and pass sufficient statistical checks, provided natively by MCNP. These checks include metrics that judge a simulations' statictical behavior and can indicate if a simulation has been run for long enough and whether the results are statistically reliable. Due to the large quantity of bins however, the uncertainties for any particular bin tends to be unacceptably high. To combat this, several iterations of a simulation with given source energy are executed, and the results combined. Each simulation provides a unique measurement of the mean behavior of each tally bin. The binned results are combined and with each iteration, uncertainty decreases.

Weighted Averaging

In the case of several measurements of the same value, the true expected fluence is a weighted average of the means from each measurement. This weighted average takes the form

$$\Phi_{\text{wav}}(\bar{\Phi}_i) = \frac{\sum_{i=1}^{n} w_i \cdot \bar{\Phi}_i}{\sum_{i=1}^{n} w_i} \tag{2.7}$$

where the weights are given by

$$w_i = \frac{1}{u(\bar{\Phi}_i)^2}. \tag{2.8}$$

2.4.4 Obtaining Distributions of Photons Generated

The F2 tally yields particle fluence normalized to surface area per source particle

$$\bar{\Phi} = \bar{\Phi}(\theta_i, E_j, S_k; E_{e^-}). \tag{2.9}$$

Where

$\theta_i =$ angle for i^{th} angle bin,

$E_j =$ energy for j^{th} energy bin,

$S_k =$ surface number for k^{th} surface,

$E_{e^-} =$ incident electron energy.

However, the use of energy and angle bins necessitates further normalization to account for differences in bin widths and the number of photons escaping the target. The number of escaping photons generated per source electron with energy E_{e^-} is the product of the fluence and surface area summed over all bins and surfaces, given by Equation 2.10. Used to obtain a probability density function describing the probability of photon emission per MeV per radian per photon scattered with Equation 2.11.

$$N(E_{e^-}) = \sum_i \sum_j \bar{\Phi}(\theta_i, E_i, S_j; E_{e^-}) \cdot A(S_j) \tag{2.10}$$

$$D(\theta, E, S; E_{e^-}) = \frac{\bar{\Phi}(\theta, E, S; E_{e^-})}{\Delta\theta \cdot \Delta E} \cdot \frac{A(S)}{N(E_{e^-})}. \tag{2.11}$$

2.4.5 Obtaining Angular Photon Distributions

The final step in obtaining probability distributions for use in the secondary source definition is to convert the normalized fluence measurements into a coordinate system where all angles are reported relative to a common axis. The most natural choice is the positive y-axis, aligned with the direction of the electron beam.

By default, MCNP records angle bins using the polar angle relative to the surface normal vector, in the positive sense of the geometric object. For the tungsten target, the positive sense for each surface aligns with the outward-facing normal vector, which is parallel to one of the coordinate axes. Surface tally measurements are split into two types: *incident* and *lateral* surfaces. Incident surfaces are those orthogonal to the y-axis, through which the beam directly passes. Lateral surfaces are aligned parallel to the beam line and are therefore defined by unit normal vectors orthogonal to the y-axis. The assigned surface names and their orientations with respect to the coordinate system are listed in Table 2.1.

Table 2.1: MCNP-assigned surface numbers, associated normal vectors, and classifications as lateral or incident.

Surface Number	Associated Positive Surface Normal	Surface Type
100.1	$+\hat{x}$	Lateral
100.2	$-\hat{x}$	Lateral
100.3	$+\hat{y}$	Incident
100.4	$-\hat{y}$	Incident
100.5	$+\hat{z}$	Lateral
100.6	$-\hat{z}$	Lateral

Because MCNP bins fluence only by polar angle relative to the surface normal, lateral surface tallies do not distinguish between photons traveling in the positive versus negative y directions. Instead, they represent conical segments of fluence, as illustrated in Figure 2.7. In this figure, a photon passing through a bin defined by angle α_2 is tallied without regard for its azimuthal direction. Although MCNP reports θ with respect to the surface normal $\hat{n}$, it does not preserve azimuthal information-meaning that photons within the same polar bin may include both forward- and backward-traveling components along $\hat{y}$. This ambiguity motivates transforming surface-based angular data into a beamline-referenced coordinate system for constructing the secondary source.

Total Photon Flux Relative to the Beamline

Angles measured from the negative incident surface and lateral surfaces undergo coordinate transformations according to Table 2.2. Lateral data are duplicated to represent both forward- and

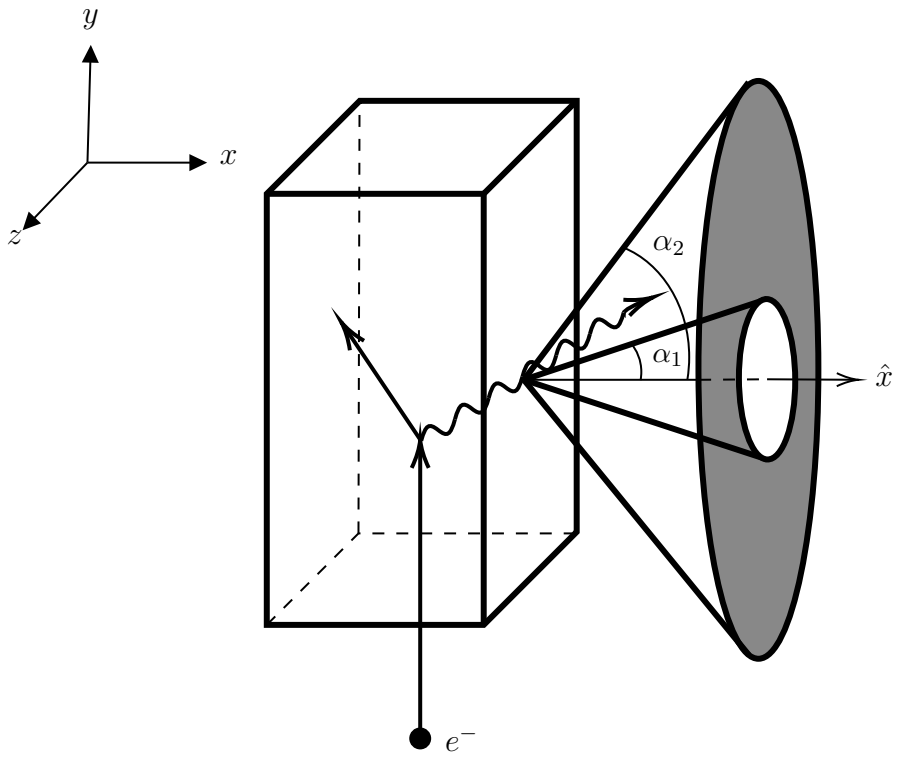

Figure 2.7: Illustration of a photon exiting surface 100.1 of the tungsten block, where the surface normal is $\hat{n}(100.1) = +\hat{x}$. The photon is recorded as contributing to the bin defined by polar angle α_2, but its azimuthal angle remains unspecified.

backward-moving photons. These are then scaled by directional weighting factors derived from the relative forward and backward flux contributions. After transformation, lateral and incident data are merged to construct a probability density function (PDF) of angles referenced to the positive y-axis. This angular transformation process is illustrated in Figure 2.8.

Table 2.2: Angular transformations applied to tally data. Lateral angles are shifted relative to the surface normal to align with the beamline direction. No transformation is needed for forward-going incident fluence.

Surface Type	Transformation
Lateral, Forward	$\theta \to \pi/2 - \theta$
Lateral, Backward	$\theta \to \pi/2 + \theta$
Incident, Forward	$\theta \to \theta$
Incident, Backward	$\theta \to \pi - \theta$

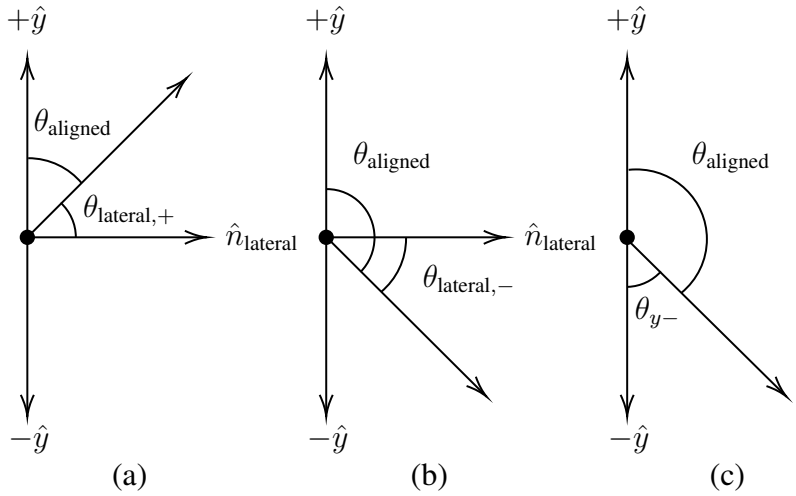

Figure 2.8: Illustration of angular rearrangement procedure. (a) Angle transformation for lateral fluences attributed to the forward direction. (b) Angle transformation for lateral fluences attributed to the backward direction. (c) Angle transformation for incident fluences through the $-\hat{y}$ surface.

The fraction of photons traveling in the forward or backward y-direction is estimated by summing the incident PDFs over all angles and normalizing to obtain directional weighting factors:

$$\begin{aligned} D(E, +\hat{y}; E_{e^-}) &= \sum_{\theta} D(\theta, E, +\hat{y}; E_{e^-}) \\ D(E, -\hat{y}; E_{e^-}) &= \sum_{\theta} D(\theta, E, -\hat{y}; E_{e^-}) \end{aligned} \tag{2.12}$$

$$\begin{aligned} f_+(E; E_{e^-}) &= \frac{D(E, +\hat{y}; E_{e^-})}{D(E, +\hat{y}; E_{e^-}) + D(E, -\hat{y}; E_{e^-})} \\ f_-(E; E_{e^-}) &= \frac{D(E, -\hat{y}; E_{e^-})}{D(E, +\hat{y}; E_{e^-}) + D(E, -\hat{y}; E_{e^-})}. \end{aligned} \tag{2.13}$$

The lateral angular-energy PDF is constructed by summing over all lateral surfaces and applying directional weights:

$$D_{\text{total}}(\theta, E, \pm xz; E_{e^-}) = \sum_{S \in \text{lateral}} D(\theta, E, S; E_{e^-}), \tag{2.14}$$

$$\begin{aligned} D(\theta, E, \pm xz; E_{e^-}) = f_+(E; E_{e^-}) \cdot D_{\text{total}}(\theta, E, \pm xz; E_{e^-}) \\ + f_-(E; E_{e^-}) \cdot D_{\text{total}}(\theta, E, \pm xz; E_{e^-}). \end{aligned} \tag{2.15}$$

Finally, the full angular-energy distribution referenced to the beamline ($+\hat{y}$) is given by:

$$D(\theta, E; E_{e^-}) = D(\theta, E, +\hat{y}; E_{e^-}) + D(\theta, E, -\hat{y}; E_{e^-}) + D(\theta, E, +xz; E_{e^-}). \tag{2.16}$$

This procedure of shifting angles, summing over lateral surfaces, and weighing by forward and backward fluence fractions makes an important assumption. This process is only valid if the distributions across lateral surfaces are uniform. In other words, there can be no bias of photon emission direction along the azimuth of the beamline from effects like polarization. This assumption is verified with a t-test:

$$t = \frac{\bar{\Phi}(\mu, E, \hat{n}_i; E_{e^-}) - \bar{\Phi}(\mu, E, \hat{n}_j; E_{e^-})}{\sqrt{u(\bar{\Phi}_i)^2 + u(\bar{\Phi}_j)^2}}, \tag{2.17}$$

where the surface unit normal vectors are antiparallel with inner-product $\hat{n}_i \cdot \hat{n}_j = -1$. The resulting t-distributions compare the fluence in each configuration of direction and energy bins through opposing lateral surfaces.

2.4.6 Angular and Energetic Probability Distributions

Two probability distributions are provided to MCNP for the secondary photon source. Angles are converted to direction cosines $\mu = cos(\theta)$ and the PDF becomes $D(\mu, E; E_{e^-})$. First, MCNP samples photon emission direction from the distribution

$$P(\mu; E_{e^-}) = \Delta\mu \cdot \int D(\mu, E; E_{e^-}) \cdot dE. \tag{2.18}$$

Where the sampled emission direction is $\mu_i \in \{\mu\}$ Once a direction is selected μ_i, the energy is determined by sampling the conditional probability distribution

$$P(E|\mu_i; E_{e^-}) = \frac{D(\mu_i, E; E_{e^-})}{P(\mu_i; E_{e^-})} \cdot \Delta\mu \cdot \Delta E. \tag{2.19}$$

That is, the probability of photon emission at energy E given an emission direction μ_i. Because the energetic probability distribution depends on direction, there is a unique $P(E|\mu_i; E_{e^-}) \, \forall \, \mu_i \in \{\mu\}$.

2.5 Input Generation and Output Processing

Input files for MCNP simulations using electron sources were generated using the Python programming language [25]. Photon distributions were analyzed and processed using the R Statistical Software [26], utilizing packages including `dplyr`, `ggplot2`, and `readr` for statistical computation and visualization.

Photon source definitions were built using a combination of R and Python, leveraging the strengths of each language: R for statistical transformations and probability density estimation, and Python for formatting outputs and generating MCNP-compliant source definitions.

MCNP output files, including surface tallies and mesh tally data, were parsed and processed using a custom Python-based parser. This parser automated extraction of tally values, uncertainty propagation, and metadata assignment for downstream analysis.

Chapter 3

Results

3.1 Checks for Lateral Photon Emission Homogeneity

Photon fluence symmetry in directions orthogonal to the beamline was evaluated by comparing emission on opposing lateral surfaces of the geometry. Two-sample t-tests were performed using Equation 2.17 to assess statistical agreement between photon fluence distributions on the $\pm x$ and $\pm z$ surfaces.

For each energy and angle bin, a t-statistic was computed comparing the corresponding fluence values on opposing surfaces. Kernel density estimate (KDE) plots of the resulting t-statistics are shown in Figures 3.1 and 3.2, with curves grouped by electron source energy.

In both lateral directions, the distributions of t-values are centered near zero across all source energies. The KDE plots provide a visual summary of the distribution shape and spread for each case, serving as a quantitative check on directional homogeneity.

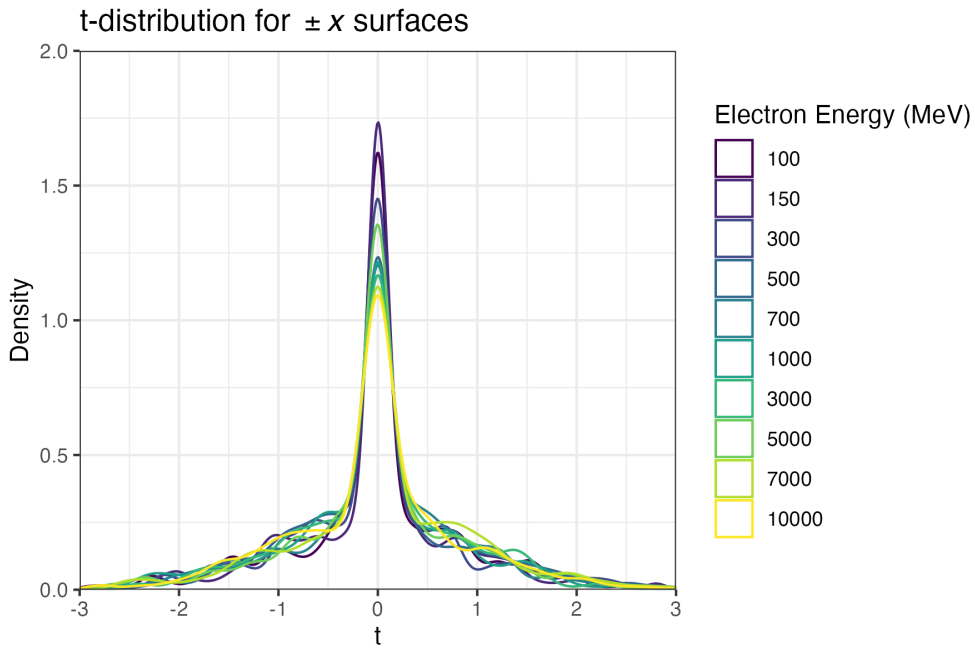

Figure 3.1: Kernel density estimate plot of t-distributions by electron source energy for $\pm x$ surfaces.

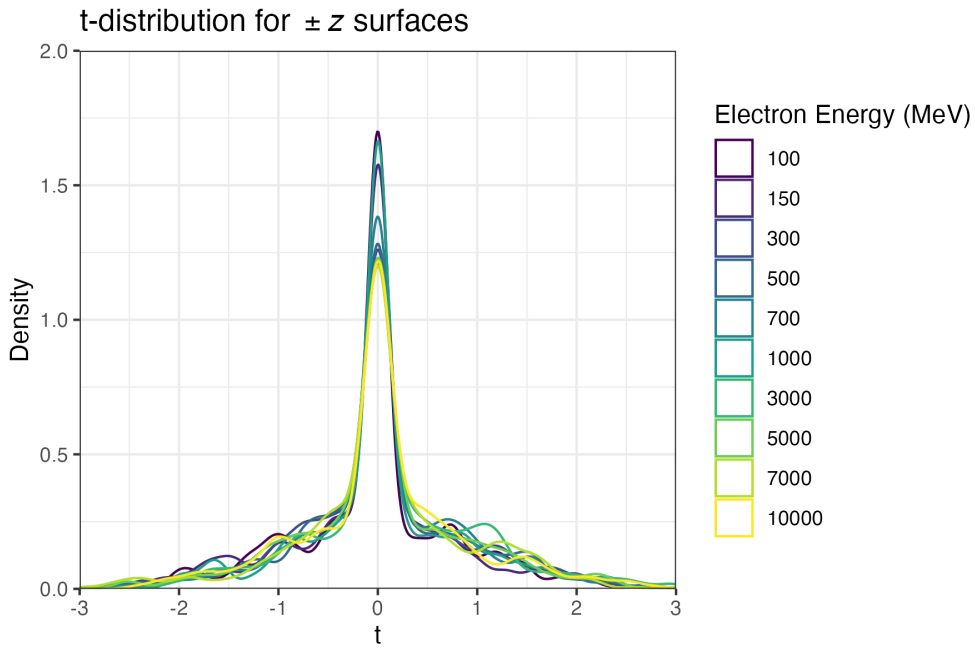

Figure 3.2: Kernel density estimate plot of t-distributions by electron source energy for $\pm z$ surfaces.

3.2 Photon Probability Distributions

Photon emission distributions are characterized in terms of energy and polar emission angle with respect to the incident electron beamline. These distributions are derived from the angle- and energy-resolved fluence data $D(\theta, E; E_{e^-})$ as defined in Equation 2.16, and are normalized to form probability density functions suitable for source definition.

3.2.1 Energy Distributions

Photon energy distributions are obtained by integrating over the emission angle and normalizing the result. The normalization constant η is defined as:

$$\eta = \iint D(\theta, E; E_{e^-})\, d\theta\, dE, \tag{3.1}$$

yielding the normalized energetic probability density function:

$$\frac{dP}{dE} = \frac{1}{\eta} \int D(\theta, E; E_{e^-})\, d\theta. \tag{3.2}$$

Figure 3.3 presents the resulting energy spectra for emitted photons. Each curve represents the normalized photon energy distribution for a specific incident electron energy, with the probability density given per MeV.

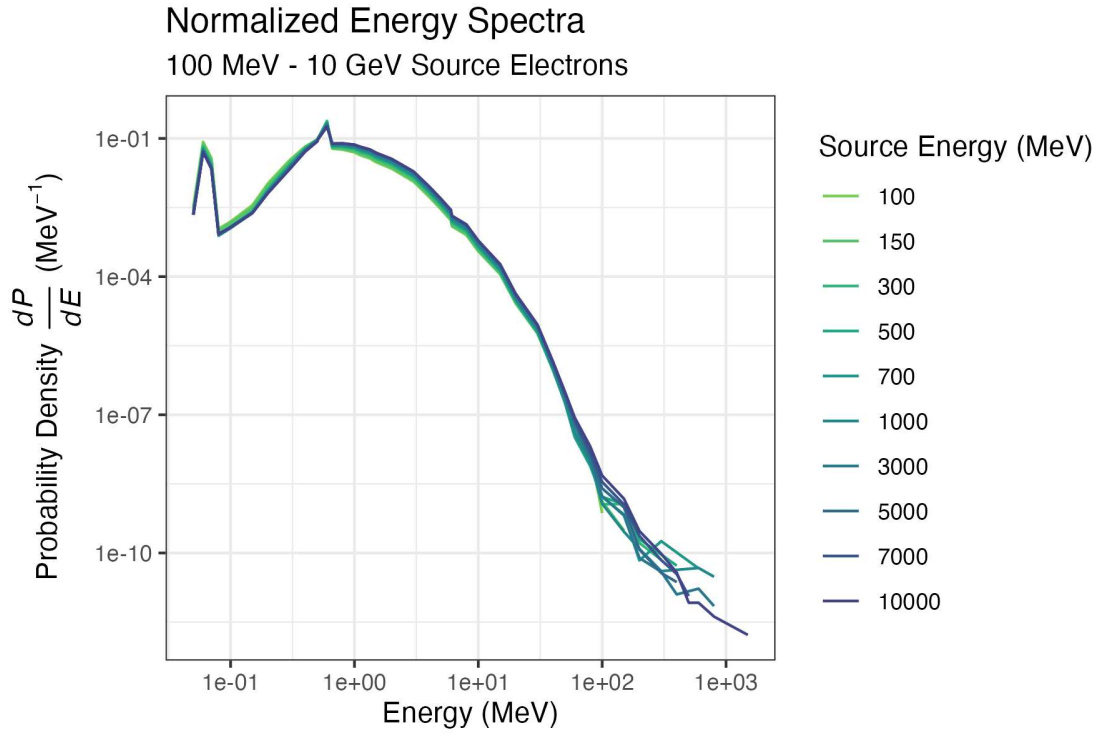

Figure 3.3: Normalized photon energy spectra, shown as probability density functions per MeV for each electron source energy.

3.2.2 Angular Distributions

Analogously, angular distributions are obtained by integrating over photon emission energy and normalizing, using the same constant η:

$$\frac{dP}{d\theta} = \frac{1}{\eta} \int D(\theta, E; E_{e^-})\, dE, \tag{3.3}$$

resulting in a normalized angular probability density function expressed per radian. These distributions describe the relative likelihood of photon emission at a given polar angle θ, measured from the beamline direction ($\theta = 0$) to the backward direction ($\theta = \pi$).

Figure 3.4 shows the angular probability density functions for each electron source energy. As before, each curve is normalized independently and colored by electron energy.

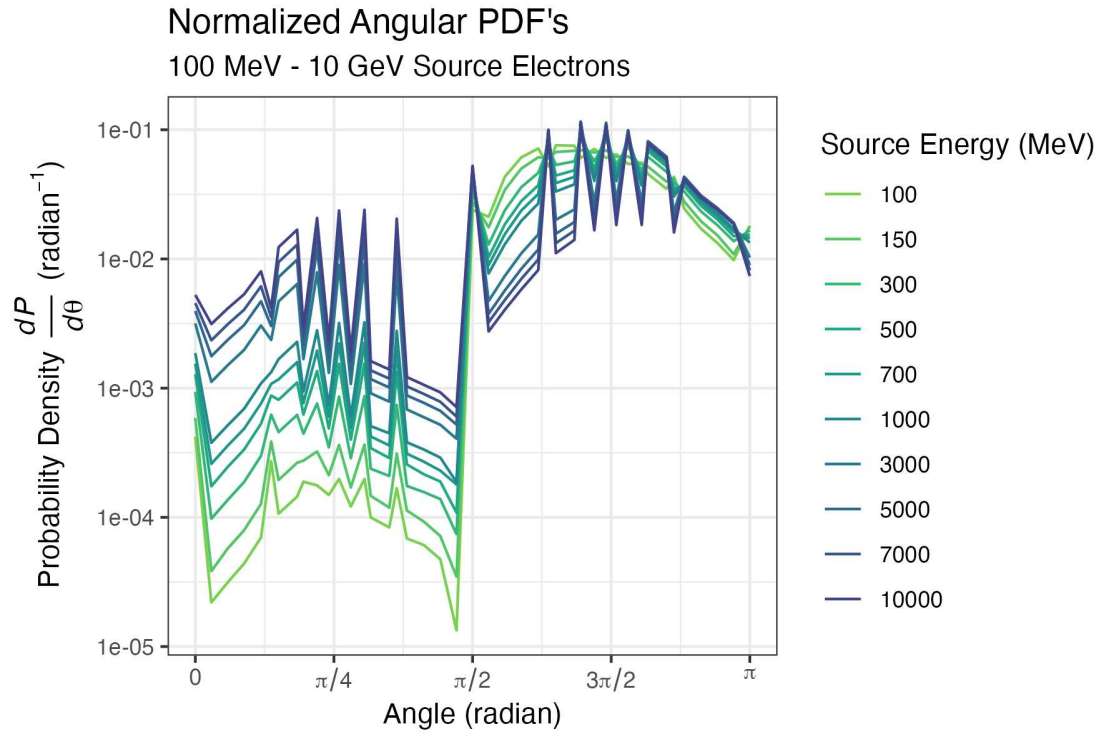

Figure 3.4: Normalized angular spectra of emitted photons, with polar emission angle ranging from 0 radians (forward, aligned with beamline) to π radians (backward, antiparallel).

3.3 Particle Production

The number of secondary particles produced per incident electron is evaluated using Equation 2.10. This value serves as a scaling factor in dose calculations, as incorporated into Equation 2.3. The same approach is applied to neutron fluence data, enabling estimation of the average number of neutrons produced per source electron.

Figure 3.5 presents the number of photons and neutrons generated per incident electron as a function of source electron energy. The results are shown on a log-log scale to capture the energy dependence across several orders of magnitude. Each data point reflects surface-integrated fluence values normalized by the total number of source histories.

As expected, photon production dominates across the entire energy range. Neutron yields, though several orders of magnitude lower, increase significantly with source energy—consistent with the onset of photonuclear reactions at higher bremsstrahlung energies.

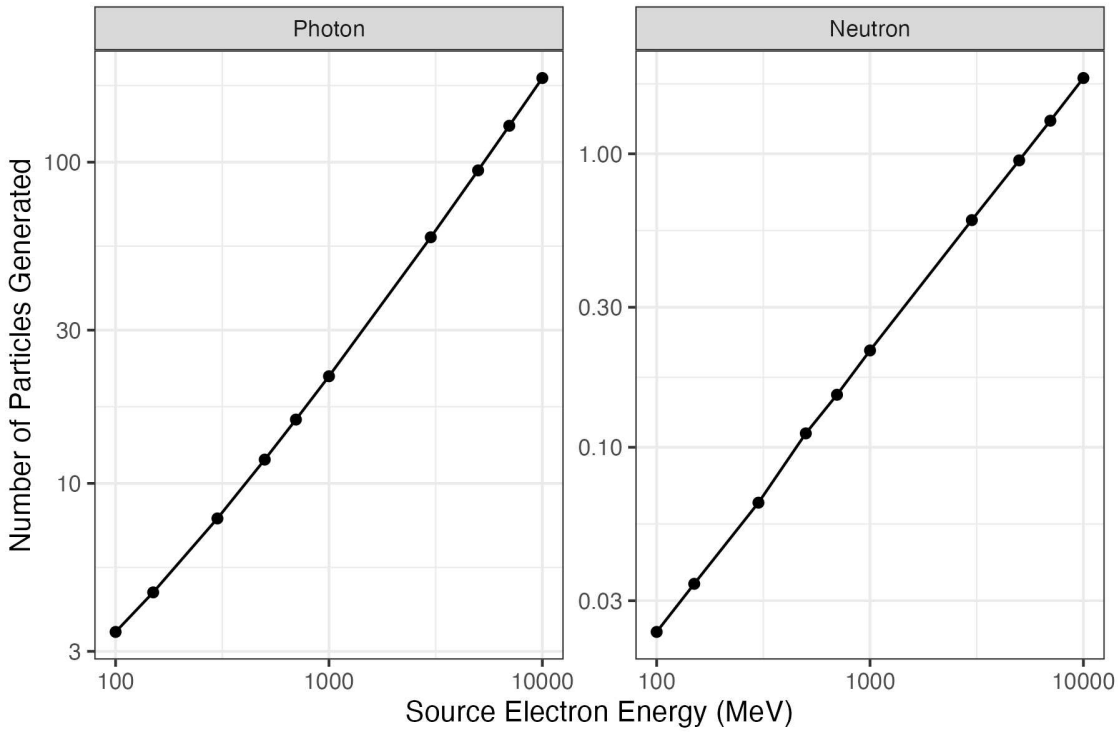

Figure 3.5: Number of secondary particles (photons and neutrons) produced per source electron entering the tungsten target.

3.4 Ambient Dose Calculations

This section presents spatial distributions of effective dose per source electron as calculated from F5 point detector tallies. These results quantify the ambient dose equivalent at various positions throughout the simulation geometry for a selection of electron source energies.

Detector coordinates and corresponding dose values are visualized in Figure 3.6, where each point represents an F5 detector placed at a specific location in the room. The plotted dose values represent the total effective dose—summed over photon and neutron contributions—for an incident electron bunch with a charge of 10 nC. These values can be readilly scaled to different bunch sizes.

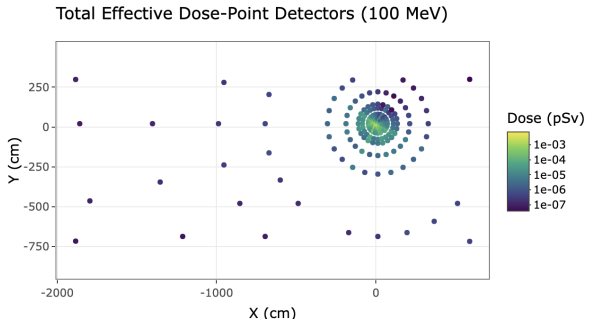

(a) 100 MeV full region

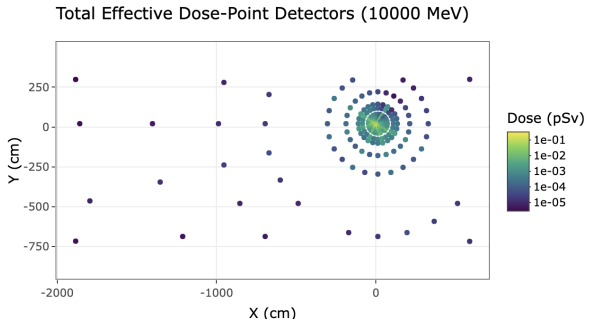

(b) 1 GeV full region

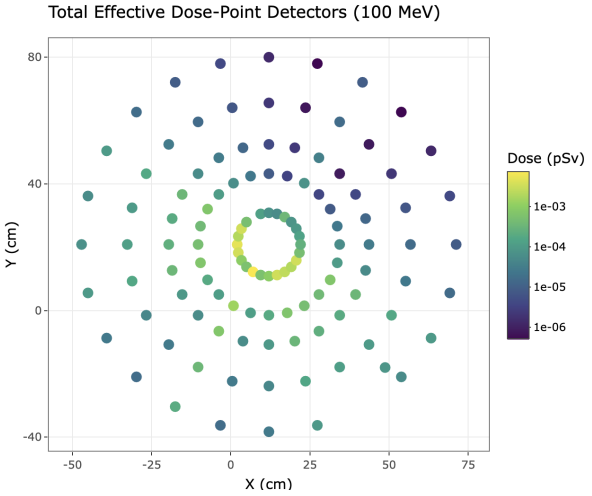

(c) 100 MeV zoomed near photon source

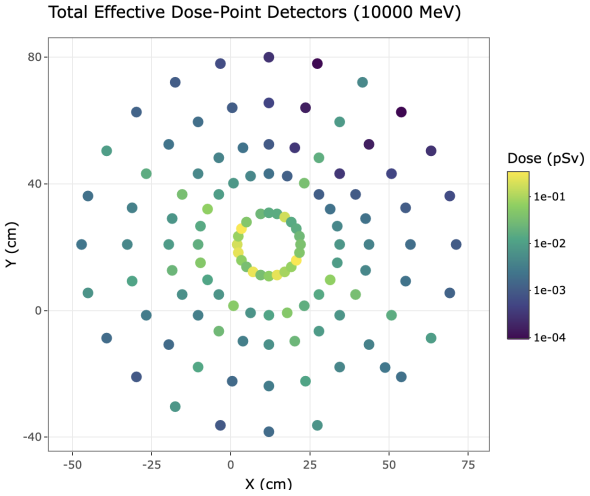

(d) 1 GeV zoomed near photon source

Figure 3.6: Total effective dose (pSv) per 10 pC electron bundle at 100 MeV and 1 GeV source energies. Top: full detector regions. Bottom: zoomed-in regions near the beamline.

Chapter 4

Discussion

4.1 Azimuthal Symmetry in Lateral Photon Emission

The results presented in Figures 3.1–3.2 demonstrate that photon production is azimuthally symmetric about the beamline axis. The t-statistic distributions peak near zero for all evaluated source energies, indicating no preferential emission direction between opposing lateral surfaces. This observation supports the assumption of uniform azimuthal emission, which is necessary for combining lateral fluence data in subsequent source definition procedures.

The sharp peaks in the t-distributions reflect that most opposing bins differ by less than one standard deviation, and nearly all differences lie within three standard deviations. This level of agreement confirms that MCNP's bremsstrahlung modeling preserves azimuthal symmetry to within statistical uncertainties. As a result, photon fluence data from the $\pm x$ and $\pm z$ surfaces can be confidently aggregated and weighted to construct a single angular-energy probability distribution for use in SDEF generation.

4.2 Probability Density Functions

4.2.1 Energy Distributions

The energetic probability density functions shown in Figure 3.3 exhibit characteristic features of photon emission from tungsten targets. Two prominent peaks are observed across all source energies.

The lower-energy peak corresponds to characteristic x-ray emission from tungsten, primarily the $K_{\alpha 1}$ and $K_{\alpha 2}$ transitions at 59.32 keV and 57.98 keV, respectively [27]. However, only a single peak is visible in the plotted spectra due to insufficient energy bin resolution. With finer binning in the region around 60 keV, these two lines would likely appear as distinct peaks.

The second prominent feature is the 511 keV annihilation peak. In the plotted distributions, this peak appears near 600 keV. This is an artifact of the binning scheme: photons with energies in the interval $(0.511 \text{ MeV}, 0.6 \text{ MeV}]$ are grouped into the 0.6 MeV bin, shifting the apparent peak center. This binning offset should be considered when using these distributions for source definition or comparison.

Beyond the annihilation peak, the spectra exhibit a smooth decline in emission probability per MeV. This behavior is consistent with bremsstrahlung emission and Compton-scattered photon production in high-Z targets. The high-energy tail of the spectrum extends to the incident electron energy, as expected, but with increasingly sparse photon production in that region.

4.2.2 Angular Distributions

While bremsstrahlung emission is generally forward-biased—especially at high electron energies—the angular spectra shown in Figure 3.4 do not exhibit a strong forward peak. Instead, a discontinuity is visible near $\theta = \pi/2$ radians (orthogonal to the beamline), where the probability density increases sharply across all electron energies. The magnitude of this discontinuity varies with electron source energy and can reach up to a few orders of magnitude between adjacent bins.

At lower electron energies (e.g., ≤ 1 GeV), the angular spectra are significantly biased toward backward emission ($\theta \approx \pi$). As the source energy increases, forward emission becomes more probable, although backward bias remains present. This trend is consistent with the expected energy dependence of bremsstrahlung angular distributions, where forward collimation strengthens with increasing electron energy.

The observed peaks and discontinuities in the angular spectra are influenced by both angular bin resolution and the procedure used to align and sum results from lateral surfaces. Only ten angular bins are defined between 0 and $\pi/2$ radians on each surface, resulting in a bin width of $\pi/20$ radians. When surface data are rotated and merged into a common coordinate system, overlapping occurs between bins from the lateral and $+\hat{y}$ or $-\hat{y}$ surfaces. These overlapping regions lead to additive effects in fluence, while non-overlapping bins contain substantially lower photon

counts. The summation process does not explicitly correct for these overlaps, introducing artificial discontinuities in the combined angular spectra.

To aid interpretation, a smoothed version of the angular distributions is provided in Figure 4.1, where a local regression model has been applied to the original data. This representation highlights general trends in photon emission directionality while suppressing binning artifacts.

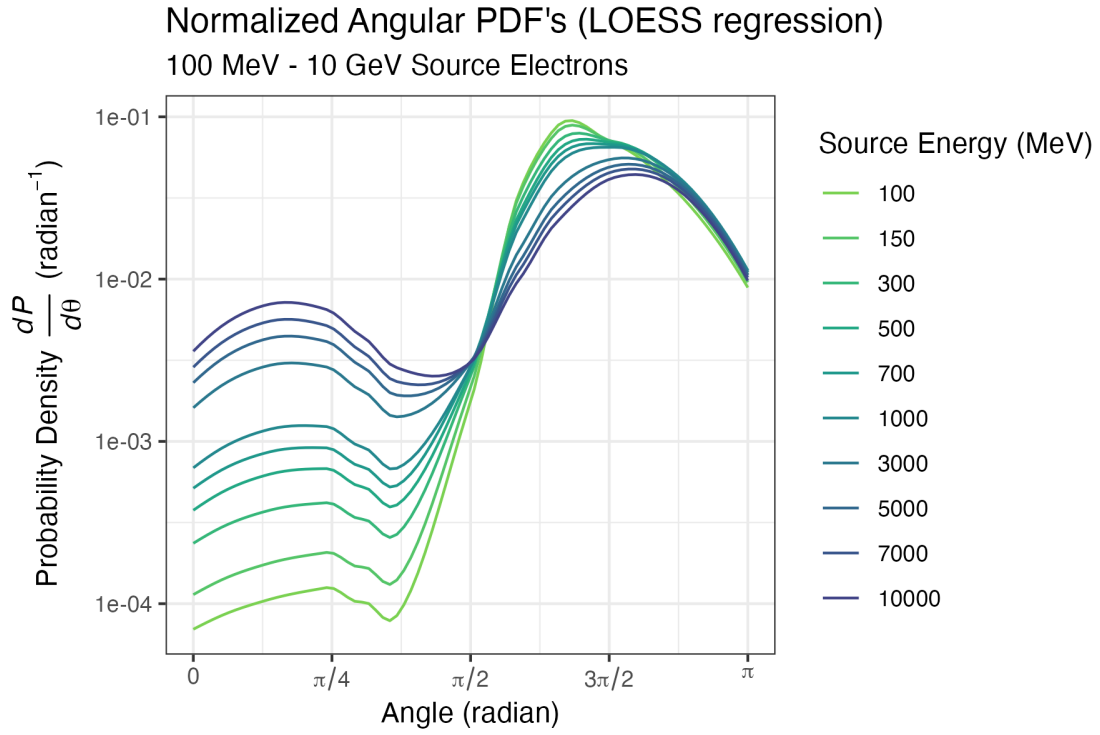

Figure 4.1: Smoothed angular spectra of emitted photons using local regression; normalized probability density per radian.

Physically, the observed backscatter enhancement can be attributed to the geometry and self-shielding properties of the tungsten target. Incident electrons strike the front face of the target, which has an area of approximately four square inches. Photons emitted in the forward direction must traverse up to four inches of high-Z material before reaching the tally surface at $+\hat{y}$, leading to significant attenuation. In contrast, photons emitted laterally pass through only one to two inches of tungsten before reaching the side tally surfaces. This discrepancy in path length results in preferential attenuation of forward-directed photons and a corresponding increase in the relative

contribution of backscattered emission. Consequently, the total fluence recorded on the exit surface is substantially lower than that on the lateral surfaces.

4.3 Particle Generation

Secondary particle production exhibits a strong dependence on the energy of the incident electron beam. As shown in Figure 3.5, the relationship between electron source energy and the number of secondary photons and neutrons produced follows an approximately linear trend on a log-log scale. This indicates a power-law dependence, suggesting that the number of secondaries increases exponentially with electron energy.

Photon production dominates across the entire energy range and increases steadily with source energy, reflecting enhanced bremsstrahlung yield at higher electron energies. Neutron production, while several orders of magnitude lower, also increases with energy due to the rising probability of photonuclear interactions, which become more prominent at higher bremsstrahlung endpoint energies.

Table 4.1 summarizes the avearge number of photons and neutrons generated per source electron at each simulated energy level. These values serve as important weighting factors for dose estimation and provide insight into the relative contributions of different radiation types in high-energy accelerator environments.

Table 4.1: Number of photons and neutrons generated per source electron.

Electron Energy (MeV)	Photons	Neutrons
100	3.45	0.0235
150	4.58	0.0343
300	7.78	0.0647
500	11.86	0.1115
700	15.80	0.1510
1000	21.56	0.2138
3000	58.38	0.5943
5000	94.29	0.9498
7000	129.82	1.2967
10000	182.78	1.8120

4.4 Dosimetry and Neutron Activation Concerns

Laser wakefield accelerators are capable of delivering ultrashort, high-current electron bunches. At Colorado State University, the ALEPH laser-plasma accelerator has demonstrated electron bunches with total charge on the order of tens of picoCoulombs, with future work planned to generate 100 pC bunches [5]. When such bunches are incident on a high-Z target such as tungsten, they generate intense bursts of secondary radiation, predominantly photons and neutrons. The resulting radiation fields raise significant concerns regarding prompt dose exposure and induced activation in nearby materials.

To evaluate the radiological implications of a typical electron bunch, dose rates were estimated under the assumption of a 10 pC bunch guided into a thick tungsten target. Using the fluence-to-dose conversion methodology discussed in Section 2.2.5, photon and neutron effective doses calculated at various points throughout the geometry are scaled by the number of photons generated per electron as discussed in Section 2.3.3. To evaluate the effective dose per 10 pC bunch, the effective doses from photons and neutrons per electron are summed and scaled by the number of electrons in a 10 pC bunch. The total number of electrons under this assumption is:

$$\begin{aligned} N_{e^-} &= \frac{q_{\text{acc}}}{e} \\ &= \frac{10\text{pC}}{1.602 \times 10^{-7}\text{pC}} \\ &= 6.24 \times 10^{7} \text{ electrons.} \end{aligned} \tag{4.1}$$

The total effective dose per 10 pC shot at various locations—such as near the beam exit, behind the beam stop, and adjacent to entryways—can be directly compared to design thresholds for radiation-controlled areas. These results are summarized in Table 4.2.

To evaluate compliance with regulatory dose limits, these per-shot effective doses may be extrapolated using the concept of *time-averaged dose equivalent rate* (TADR), as described in NCRP Report No. 151 [28]. This quantity is used in shielding design to ensure that radiation exposure limits are not exceeded over operational timeframes, even when the radiation is delivered in brief

Table 4.2: Estimated total effective dose (pSv) per 10 pC monoenergetic electron bundle, by detector position and source energy. Note that the beam is directed 60° north of east. Energies are given in MeV.

Energy (MeV)	Mid-Beamline	Posterior to Beamstop	NE Entry	NW Entry	SW Entry
100	2.07E2	4.85E0	2.69E0	4.26E0	7.11E0
150	3.53E2	6.41E0	3.90E0	8.68E0	5.14E0
300	8.86E2	1.27E1	6.45E0	1.15E1	9.77E0
500	1.80E3	2.07E1	4.57E2	2.14E1	1.90E1
700	2.89E3	2.45E1	1.63E1	2.13E1	2.39E1
1000	4.60E3	3.50E1	2.80E1	3.23E1	2.99E1
3000	2.11E4	1.05E2	1.05E2	6.92E1	8.53E1
5000	4.16E4	1.95E2	1.92E2	1.25E2	1.49E2
7000	6.54E4	2.78E2	7.59E2	1.34E2	2.06E2
10000	1.05E5	3.84E2	5.06E2	1.90E2	2.41E2

pulses. In pulsed accelerator facilities, TADR is proportional to the *instantaneous dose equivalent rate* (IDR) and incorporates operational parameters that account for frequency and geometry of beam use.

TADR is defined by:

$$R_w = \frac{IDR \cdot W_{\text{pri}} \cdot U_{\text{pri}}}{\dot{D}_0}, \tag{4.2}$$

where:

R_w: Time-averaged dose equivalent rate, averaged over a week.

IDR: Instantaneous dose equivalent rate, based on a typical short-term (20–60 s) operational average.

W_{pri}: Weekly workload, the number of Gray delivered per week at 1 meter from the source.

U_{pri}: Use factor, the fraction of time the primary beam is directed toward a given barrier.

$\dot{D}_0$: Dose output rate at 1 meter from the source.

This formulation allows for the translation of per-shot or pulsed dose data into quantities that can be directly compared with regulatory design limits. For example, areas accessible to the public

are generally limited to 0.02 mSv/h (unrestricted area limit), while controlled areas for occupational exposure are limited to 0.1 mSv/week. Using Equation 4.2, designers can scale measured or simulated per-shot doses by repetition rate and beam usage patterns to verify compliance.

This consideration is especially important in the context of high-charge laser-driven accelerators such as ALEPH. Even at relatively low repetition rates (e.g., 0.01–1 Hz), accumulated doses near the target or along direct beam paths can exceed design thresholds if shielding is inadequate. Furthermore, since many shielding requirements are driven not by individual shots but by time-integrated exposure over hours or weeks, incorporating TADR into dose analysis provides a conservative, regulation-compliant framework for safe facility operation.

In addition to prompt dose, the neutron component introduces the potential for material activation, particularly in structural components and diagnostics located near the target. Although neutron fluence is significantly lower than photon fluence, its higher biological weighting and activation potential warrant careful design considerations. Neutron shielding, delayed dose monitoring, and access controls may be required depending on facility layout and repetition rate.

Chapter 5

Conclusion

Laser wakefield acceleration is a promising technique with wide-ranging applications across high-energy physics. As with any emerging technology-particularly one operating in high-radiation regimes-there is a pressing need to evaluate the radiological protection requirements associated with deployment. This thesis presented a simulation-based study of secondary radiation production from high energy electron beams interacting with a tungsten target, representing a plausible experimental scenario at the Advanced Beam Laboratory at Colorado State University. Photon spectra were computed from electron interactions using MCNP for the purposes of producing a secondary source term, used in dose estimation. The energy spectra revealed characteristic tungsten K-shell X-ray and annihilation peaks, followed by typical spectral behavior up to the total source electron energy. Angular spectra were constructed which display typical behavior of bremsstrahlung emission. As expected, electrons of higher energy produce spectra with a forward bias relative to the spectra from low energy electrons. Although some limitations in the directional sampling methodology introduced potential artifacts in certain emission directions, these spectra nevertheless formed the basis for secondary source definitions, enabling dose estimation in downstream simulations that model the propagation and interactions of photon radiation through a simplified facility layout.

One ancillary finding is that of the average photon and neutron yield per source electron across the simulated energy range. These data provide a valuable strategy for scaling dose estimates in downstream simulations. Both photon and neutron yield were found to apparently increase exponentially with increasing electron energy, although this claim requires validation through future application of linear regression modeling to log-transformed data.

Through the application of the photon emission spectra in secondary MCNP simulations, preliminary estimations of total effective radiation dose at various points of interest in the simulation

geometry have been established and, with sufficient care, hold applications in estimating dose rates and shielding requirements in the Advanced Beam Lab at Colorado State University.

Many radiation transport codes exist that are well-suited for a study of wake field acceleration. MCNP was chosen for its maturity and strong track record in radiation protection and shielding studies. Its extensive, validated cross-section libraries-particularly for neutron interactions-make it a powerful tool for many radiological applications. However, MCNP exhibits notable limitations, particularly at multi-GeV energies, especially in modeling exotic secondary radiation. Despite the significant library of high-energy physics models, MCNP may require further validation and benchmarking with respect to high-energy electron transport, as discussed in 1.4.2.

Other Monte Carlo codes such as FLUKA may offer complimentary capabilities. FLUKA maintains an extensive track record of use at CERN for meson transport and interaction studies. The results of an MCNP-based study would surely benefit by benchmarking against a similar study through FLUKA.

The two-source method applied to this work involves stitched angular-energy distribution, where photon emission spectra from the six target surfaces are combined into a single composite source. While practical, this method introduces assumptions about the continuity of emission behavior and angular correlations that may inadequately reflect true physics. Studying the contributions of each surface individually, while more computationally expensive, may aid in improving angular fidelity. Another important extension of this work should involve benchmarking present dose estimates against simulations that transport the primary electron beam directly. Such studies would help quantify the accuracy of the photon-only model used in this study and the contribution of charged particles to dose. This comparison would provide further insight into dose contributions missed by photon-based tallies, and inform decisions about when simplified models are appropriate, despite the increased computational demand.

To validate the simulated dose maps, future studies should include experimental dosimetry using techniques including track-etch dosimeters and radiotherapy film for neutrons, and passive dosimetry with properly calibrated instrumentation. This calibration would necessarily begin with

energy spectra obtained through simulations. Of course, dosimetry must be passive due to the short-pulsed nature of the radiation fields.

While this study focused specifically on the LWFA use case at Colorado State University, the methods and findings are broadly applicable to any compact high-energy electron source, such as those found in medical accelerators. The modular nature of the secondary photon source generation pipeline supports reuse in other simulation workflows, and the findings highlight the importance of integrating shielding and dosimetry considerations in early accelerator design.

References

[1] S. Lüders, R. Horisberger, and O. S. Brüning, eds. *The Large Hadron Collider: A Marvel of Technology*. CERN Publication. Lausanne: EPFL Press, 2008. URL: https://cds.cern.ch/record/1129806.

[2] Christian Bohm et al. *Dosimetry in Environments Surrounding a Laser Plasma Accelerator*. Tech. rep. SSM Report 2019:04. Accessed: 2025-02-25. Swedish Radiation Safety Authority, 2019.

[3] Edmund Wilson. *An Introduction to Particle Accelerators*. Oxford, UK: Oxford University Press, 2001. ISBN: 0-19-850829-8.

[4] T. Tajima and J. M. Dawson. "Laser Electron Accelerator". In: *Physical Review Letters* 43.4 (July 23, 1979), pp. 267–270. ISSN: 0031-9007. DOI: 10.1103/PhysRevLett.43.267. (Visited on 01/13/2025).

[5] B. Miao et al. "Multi-GeV Electron Bunches from an All-Optical Laser Wakefield Accelerator". In: *Physical Review X* 12.3 (Sept. 16, 2022), p. 031038. ISSN: 2160-3308. DOI: 10.1103/PhysRevX.12.031038. (Visited on 04/21/2024).

[6] Colorado State University. *Work to Start on Powerful New Laser Facility Funded by Public-Private Partnership*. 2024. URL: https://source.colostate.edu/work-to-start-on-powerful-new-laser-facility-funded-by-public-private-partnership/.

[7] Colorado State University. *Laboratory for Advanced Lasers and Extreme Photonics (L-ALEPH)*. URL: https://lasers.colostate.edu/.

[8] K. Pepitone et al. "The Electron Accelerators for the AWAKE Experiment at CERN—Baseline and Future Developments". In: *Nuclear Instruments and Methods in Physics Research Section A* 909 (Nov. 2018), pp. 102–106. ISSN: 0168-9002. DOI: 10.1016/j.nima.2018.02.044. (Visited on 02/23/2025).

[9] Michael C. Downer, Nabil Hafz, et al. *Advanced Lasers for Accelerators at Colorado State University*. Presentation at CLASSE Workshop on Advanced Accelerators. 2024. URL: https://indico.classe.cornell.edu/event/2108/contributions/2221/.

[10] J. E. Turner. *Atoms, Radiation, and Radiation Protection*. 3rd ed. Physics Textbook. OCLC: 82672521. Weinheim: Wiley-VCH, 2007. ISBN: 978-3-527-40606-7.

[11] Frank H. Attix. *Introduction to radiological physics and radiation dosimetry*. en. New York: Wiley, 1986. ISBN: 978-0-471-01146-0.

[12] Armen Apyan, Mieczyslaw Krasny, and Wiesław Płaczek. "Gamma Factory High-Intensity Muon and Positron Source: Exploratory Studies". In: (Dec. 2022). DOI: 10.48550/arXiv.2212.06311. arXiv: 2212.06311 [hep-ex]. URL: https://arxiv.org/abs/2212.06311 (visited on 05/19/2025).

[13] Joel Kulesza et al. *MCNP® Code Version 6.3.0 Theory & User Manual*. Tech. rep. LA-UR-22-30006. Los Alamos National Laboratory, Sept. 28, 2022. DOI: 10.2172/1889957.

[14] International Commission on Radiological Protection. "The 2007 Recommendations of the International Commission on Radiological Protection". In: *Annals of the ICRP*. ICRP Publication 103.2–4 (2007), pp. 1–332. ISSN: 0146-6453. DOI: 10.1016/j.icrp.2007.10.003. URL: https://doi.org/10.1016/j.icrp.2007.10.003.

[15] Glenn F. Knoll. *Radiation Detection and Measurement*. 4th ed. Hoboken, NJ: John Wiley & Sons, 2010. ISBN: 9780470131480. (Visited on 05/12/2025).

[16] ICRP. "Conversion Coefficients for Radiological Protection Quantities for External Radiation Exposures". In: *Annals of the ICRP* 40.2–5 (2010).

[17] Thomas E. Johnson. *Introduction to Health Physics*. 5th. McGraw-Hill Education, 2017. ISBN: 978-0-07-183527-5.

[18] H. Grady Hughes. "Improvements in Electron-Photon-Relaxation Data for MCNP6". In: *EPJ Web of Conferences* 153 (2017). Ed. by F. Malvagi et al. DOI: 10.1051/epjconf/201715306009.

[19] C. Anderson et al. “Delta-Ray Production in MCNP 6.2.0”. In: *Physics Procedia* (2017). ISSN: 1875-3892. DOI: 10.1016/j.phpro.2017.09.001.

[20] H. Grady Hughes. “Enhanced Electron-Photon Transport in MCNP6”. In: *SNA + MC 2013 - Joint International Conference on Supercomputing in Nuclear Applications + Monte Carlo*. Ed. by D. Caruge et al. Paris, France: EDP Sciences, 2014. ISBN: 978-2-7598-1269-1. DOI: 10.1051/snamc/201403105. (Visited on 04/26/2025).

[21] David A. Dixon and H. Grady Hughes. “Validation of the MCNP6 Electron-Photon Transport Algorithm: Multiple-Scattering of 13- and 20-MeV Electrons in Thin Foils”. In: *EPJ Web of Conferences* 153 (2017). Ed. by F. Malvagi et al., p. 06021. ISSN: 2100-014X. DOI: 10.1051/epjconf/201715306021. (Visited on 04/26/2025).

[22] Rebecca S. Detwiler et al. *Compendium of Material Composition Data for Radiation Transport Modeling*. Tech. rep. 200-DMAMC-128170, PNNL-15870, Rev. 2. Pacific Northwest National Laboratory, 2021. DOI: 10.2172/1782721.

[23] National Institute of Standards and Technology. *NIST Material Composition Database*. Accessed: 2025-04-21. 2025.

[24] Jeremy Lloyd Conlin. *Listing of Available ACE Data Tables*. Tech. rep. LA-UR-17-20709. Los Alamos National Laboratory, 2017. DOI: 10.2172/1342828.

[25] Python Software Foundation. *Python 3 Reference Manual*. Version 3.x. 2024. URL: https://www.python.org.

[26] R Core Team. *R: A Language and Environment for Statistical Computing*. R Foundation for Statistical Computing. Vienna, Austria, 2024. URL: https://www.R-project.org/.

[27] National Institute of Standards and Technology. *X-ray Transition Energies Database (Version 1.3)*. NIST Standard Reference Database 128. NIST Physical Measurement Laboratory. 2020. URL: https://physics.nist.gov/PhysRefData/XrayTrans/.

[28] National Council on Radiation Protection and Measurements. *Structural Shielding Design and Evaluation for Megavoltage X- and Gamma-Ray Radiotherapy Facilities*. NCRP Report No. 151. Bethesda, MD: NCRP Publications, 2005.

Appendix A

Data

Table A.1: Isotopic composition of materials used in MCNP by nuclide and atom fraction.

Material	Mass Density (g/cm^3)	Nuclide	Atom Fraction
Air (Dry, Near Sea-Level)	0.001205	^{12}C	1.23E-04
		^{13}C	1.00E-06
		^{14}N	7.52E-01
		^{15}N	2.94E-03
		^{16}O	2.31E-01
		^{17}O	9.40E-05
		^{18}O	5.35E-04
		^{36}Ar	0.000043
		^{38}Ar	0.000008
		^{40}Ar	0.012776
Gypsum	2.32	^{1}H	0.023411
		^{2}H	0.000005
		^{16}O	0.556044
		^{17}O	0.000225
		^{18}O	0.001286
		^{32}S	0.185318
		^{33}S	0.0014
		^{34}S	0.00792
		^{36}S	0.000019
		^{40}Ca	0.225655
		^{42}Ca	0.001506

Continued on next page

(Continued from previous page)

Material	Mass Density (g/cm^3)	Nuclide	Atom Fraction
		^{43}Ca	0.000314
		^{44}Ca	0.004856
		^{46}Ca	0.000009
		^{48}Ca	0.000435
Concrete	2.23	^{1}H	0.004529
		^{2}H	0.000001
		^{16}O	0.511211
		^{17}O	0.000207
		^{18}O	0.001182
		^{28}Si	0.332335
		^{29}Si	0.016883
		^{30}Si	0.011142
		^{27}Al	0.03555
		^{23}Na	0.01527
		^{40}Ca	0.056139
		^{42}Ca	0.000347
		^{43}Ca	0.000058
		^{44}Ca	0.001208
		^{46}Ca	0.000002
		^{48}Ca	0.000108
		^{54}Fe	0.000805
		^{56}Fe	0.012644
		^{57}Fe	0.000292
		^{58}Fe	0.000039

Continued on next page

(Continued from previous page)

Material	Mass Density (g/cm^3)	Nuclide	Atom Fraction
Tungsten	19.3	^{180}W	0.0012
		^{182}W	0.265
		^{183}W	0.1431
		^{184}W	0.3064
		^{186}W	0.2843
Aluminum	2.6989	^{27}Al	1
Polyethylene, Non-Borated	0.93	^{1}H	0.143686
		^{2}H	0.000033
		^{12}C	0.847114
		^{13}C	0.009162

Table A.2: Photonuclear cross-section library information for materials.

Material	ZAID	PNLIB	Extension	Min Energy (MeV)	Max Energy (MeV)
^{1}H	1001	N/A	N/A	N/A	N/A
^{2}H	1002	ENDF7u	.70u	2.2246	30
^{12}C	6012	ENDF7u	.70u	3.366593	150
^{13}C	6013	ENDF7u	.70u	4.9463	140
^{14}N	7014	ENDF7u	.70u	7.5506	130
^{15}N	7015	ENDF7u	.70u	10.95999	140
^{16}O	8016	ENDF7u	.70u	12.49999	150
^{17}O	8017	ENDF7u	.70u	4.499996	140
^{18}O	8018	ENDF7u	.70u	6.23	140
^{23}Na	11023	ENDF7u	.70u	8.7941	140
^{27}Al	13027	ENDF7u	.70u	8.499992	150

Continued on next page

(Continued from previous page)

Material	ZAID	PNLIB	Extension	Min Energy (MeV)	Max Energy (MeV)
^{28}Si	14028	ENDF7u	.70u	9.9843	150
^{29}Si	14029	ENDF7u	.70u	8.4739	140
^{30}Si	14030	ENDF7u	.70u	10.6096	140
^{32}S	16032	ENDF7u	.70u	6.9484	140
^{33}S	16033	ENDF7u	.70u	7.1161	140
^{34}S	16034	ENDF7u	.70u	7.923699	140
^{36}S	16036	ENDF7u	.70u	9.008099	140
^{36}Ar	18036	ENDF7u	.70u	6.6392	140
^{38}Ar	18038	ENDF7u	.70u	7.2076	140
^{40}Ar	18040	ENDF7u	.70u	6.7998	140
^{40}Ca	20040	ENDF7u	.70u	7.0403	150
^{42}Ca	20042	ENDF7u	.70u	6.2568	140
^{43}Ca	20043	ENDF7u	.70u	7.5925	140
^{44}Ca	20044	ENDF7u	.70u	8.855	140
^{46}Ca	20046	ENDF7u	.70u	10.3993	140
^{48}Ca	20048	ENDF7u	.70u	9.9399	140
^{54}Fe	26054	ENDF7u	.70u	8.4179	140
^{56}Fe	26056	ENDF7u	.70u	7.6142	150
^{57}Fe	26057	ENDF7u	.70u	7.3209	140
^{58}Fe	26058	ENDF7u	.70u	7.6466	140
^{180}W	74180	ENDF7u	.70u	4.999999	30
^{182}W	74182	ENDF7u	.70u	4.999999	30
^{183}W	74183	ENDF7u	.70u	3.999999	30
^{184}W	74184	ENDF7u	.70u	7.499999	150

Continued on next page

(Continued from previous page)

Material	ZAID	PNLIB	Extension	Min Energy (MeV)	Max Energy (MeV)
^{186}W	74186	ENDF7u	.70u	4.999999	30
^{204}Pb	82204	N/A	N/A	N/A	N/A
^{206}Pb	82206	ENDF7u	.70u	8	150
^{207}Pb	82207	ENDF7u	.70u	6.5	150
^{208}Pb	82208	ENDF7u	.70u	7.499999	150

Table A.3: Nuclear cross-section library information for materials.

Material	ZAID	NLIB	Extension	Temp (K)	Max. Energy (MeV)	GPD
^{1}H	1001	endf66a	.66c	293.6	150	yes
^{2}H	1002	endf70a	.70c	293.6	150	yes
^{12}C	6012	100xs	.21c	300	100	yes
^{13}C	6013	N/A	N/A	N/A	N/A	N/A
^{14}N	7014	endf70a	.70c	293.6	150	yes
^{15}N	7015	endf70a	.70c	293.6	20	yes
^{16}O	8016	endf70a	.70c	293.6	150	yes
^{17}O	8017	endf70a	.70c	293.6	20	no
^{18}O	8018	N/A	N/A	N/A	N/A	N/A
^{23}Na	11023	ednf70a	.70c	293.6	20	yes
^{27}Al	13027	endf70a	.70c	293.6	150	yes
^{28}Si	14028	endf70a	.70c	293.6	150	yes
^{29}Si	14029	endf70a	.70c	293.6	150	yes
^{30}Si	14030	endf66a	.66c	293.6	150	yes
^{32}S	16032	endf66a	.66c	293.6	20	yes
^{33}S	16033	endf70a	.70c	293.6	20	yes

Continued on next page

(Continued from previous page)

Material	ZAID	NLIB	Extension	Temp (K)	Max. Energy (MeV)	GPD
^{34}S	16034	endf70a	.70c	293.6	20	yes
^{36}S	16036	endf70a	.70c	293.6	20	yes
^{36}Ar	18036	endf70a	.70c	293.6	20	no
^{38}Ar	18038	endf70a	.70c	293.6	20	no
^{40}Ar	18040	endf70a	.70c	293.6	20	no
^{40}Ca	20040	endf70a	.70c	293.6	200	yes
^{42}Ca	20042	endf70a	.70c	293.6	200	yes
^{43}Ca	20043	endf70a	.70c	293.6	200	yes
^{44}Ca	20044	endf70a	.70c	293.6	200	yes
^{46}Ca	20046	endf70a	.70c	293.6	200	yes
^{48}Ca	20048	endf70a	.70c	293.6	200	yes
^{54}Fe	26054	endf70a	.70c	293.6	150	yes
^{56}Fe	26056	endf70a	.70c	293.6	150	yes
^{57}Fe	26057	endf70a	.70c	293.6	150	yes
^{58}Fe	26058	endf70a	.70c	293.6	20	yes
^{180}W	74180	ednf71x	.80c	293.6	150	yes
^{182}W	74182	endf70i	.70c	293.6	150	yes
^{183}W	74183	endf70i	.70c	293.6	150	yes
^{184}W	74184	endf70i	.70c	293.6	150	yes
^{186}W	74186	endf70i	.70c	293.6	150	yes
^{204}Pb	82204	endf70i	.70c	293.6	200	yes
^{206}Pb	82206	endf70i	.70c	293.6	200	yes
^{207}Pb	82207	endf70i	.70c	293.6	200	yes
^{208}Pb	82208	endf70i	.70c	293.6	150	yes

Table A.4: Effective dose per fluence for mono-energetic photons incident on anteroposterior geometry.

Energy (MeV)	pSv cm^2
0.01	0.0685
0.015	0.156
0.02	0.225
0.03	0.313
0.04	0.351
0.05	0.37
0.06	0.39
0.07	0.413
0.08	0.444
0.1	0.519
0.15	0.748
0.2	1
0.3	1.51
0.4	2
0.5	2.47
0.511	2.52
0.6	2.91
0.662	3.17
0.8	3.73
1	4.49
1.117	4.9
1.33	5.59
1.5	6.12
2	7.48

Continued on next page

(Continued from previous page)

Energy (MeV)	pSv cm^2
3	9.75
4	11.7
5	13.4
6	15
6.129	15.1
8	17.8
10	20.5
15	26.1
20	30.8
30	37.9
40	43.1
50	47.1
60	50.1
80	54.5
100	57.8
150	63.3
200	67.3
300	72.3
400	75.5
500	77.5
600	78.9
800	80.5
1000	81.7
1500	83.8

Continued on next page

(Continued from previous page)

Energy (MeV)	pSv cm^2
2000	85.2
3000	86.9
4000	88.1
5000	88.9
6000	89.5
8000	90.2
10000	90.7

Table A.5: Effective dose per fluence for mono-energetic neutrons incident on anteroposterior geometry.

Energy (MeV)	pSv cm^2
1.0e-09	3.09
1.0e-08	3.55
2.5e-08	4.00
1.0e-07	5.20
2.0e-07	5.87
5.0e-07	6.59
1.0e-06	7.03
2.0e-06	7.39
5.0e-06	7.71
1.0e-05	7.82
2.0e-05	7.84
5.0e-05	7.82
1.0e-04	7.79
2.0e-04	7.73

Continued on next page

(Continued from previous page)

Energy (MeV)	pSv cm^2
5.0e-04	7.54
0.001	7.54
0.002	7.61
0.005	7.97
0.01	9.11
0.02	12.2
0.03	15.7
0.05	23.0
0.07	30.6
0.1	41.9
0.15	60.6
0.2	78.8
0.3	114
0.5	177
0.7	232
0.9	279
1.0	301
1.2	330
1.5	365
2.0	407
3.0	458
4.0	483
5.0	494
6.0	498

Continued on next page

(Continued from previous page)

Energy (MeV)	pSv cm^2
7.0	499
8.0	499
9.0	500
10.0	500
12.0	499
14.0	495
15.0	493
16.0	490
18.0	484
20.0	477
21.0	474
30.0	453
50.0	433
75.0	420
100.0	402
130.0	382
150.0	373
180.0	363
200	359
300	363
400	389
500	422
600	457
700	486

Continued on next page

(Continued from previous page)

Energy (MeV)	pSv cm^2
800	508
900	524
1000	537
2000	612
5000	716
10000	933